Computational Discovery of Novel Semiconductors for Beyond-Si Photovoltaics

A Thesis

submitted to

Indian Institute of Science Education and Research Pune in partial fulfilment of the requirements for the BS-MS Dual Degree Programme

by

Avaneesh B

Indian Institute of Science Education and Research Pune

Dr. Homi Bhabha Road,

Pashan, Pune 411008, INDIA.

April, 2025

Supervisor: Dr Sai Gautam Gopalakrishnan

Avaneesh B

Certificate

This is to certify that this dissertation entitled **Computational Discovery of Novel Semiconductors for Beyond-Si Photovoltaics** towards the partial fulfilment of the BS-MS dual degree programme at the Indian Institute of Science Education and Research, Pune represents study/work carried out by Avaneesh B at Indian Institute of Science Education and Research under the supervision of Dr. Sai Gautam Gopalakrishnan, Assistant Professor, Department of Materials Engineering, Indian Institute of Science (IISc) during the academic year 2024-2025.

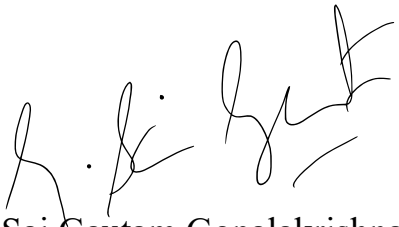

Dr. Sai Gautam Gopalakrishnan

Committee:

Dr. Sai Gautam Gopalakrishnan

Dr. Prasenjit Ghosh

This thesis is dedicated to my omniscient preceptor, my parents Mrs Lakshmi Balasubramanian and Mr Balasubramanian, and my late *paati* Smt. Rama Venkataraman

Declaration

I hereby declare that the matter embodied in the report entitled "Computational Discovery of Novel Semiconductors for Beyond-Si Photovoltaics" are the results of the work carried out by me at the Department of Chemistry, Indian Institute of Science Education & Research (IISER) Pune, under the supervision of Dr. Sai Gautam Gopalakrishnan, and the same has not been submitted elsewhere for any other degree. Wherever others contribute, every effort is made to indicate this clearly, with due reference to the literature and acknowledgement of collaborative research and discussions.

Avaneesh B

20201011

Table of Contents

List of Tables

List of Figures

Abstract

Novel and efficient solar cell materials are required to balance the energy needs of the constantly growing population. Given the disadvantages of silicon solar cells, in this study, we perform computational investigation and scanning of pnictide compounds (phosphides and nitrides) to evaluate their ability to be used as prospective beyond-Silicon solar cell materials. We postulate crystal structures for redox-inactive, non-toxic and relatively unexplored chemical space of $ABCX_2$, $BB'B''X_2$ and A_4BX_2 (A = Li, Na, K; B = Ca, Sr, Mg, Zn; C = Al, Ga, In; X = N, P) composition classes based on experimentally stable compounds and employ Density Functional Theory to compute their equilibrium structures, polymorph stability, compositional stability (0K convex hull diagram), electronic properties (density of states, band structure and effective mass) and intrinsic defect formation energies to filter these compounds based on criteria set on all the above properties for declaring them as suitable candidates for beyond-Si photovoltaic materials.

Upon evaluating the above-mentioned properties for the eight compositions in the $BB'B''X_2$ class, 24 compositions in the A_4BX_2 class and 72 compositions in the $ABCX_2$ class, we find that 31 compositions are stable or metastable with the postulated structures, and four compounds viz. K_4ZnP_2, Na_4ZnP_2 of the R-3mH space group and $NaSrInN_2$ and $NaCaInN_2$ of the $P2_1/c$ space group have optimal direct (or nearest direct) bandgaps and resist forming intrinsic defects. Therefore, we propose that these compounds can be prospective candidates for the utility in beyond-Si photovoltaic materials.

Acknowledgements

First, I would like to thank my supervisor, Dr. Sai Gautam Gopalakrishnan (Sai sir) for his constant and constructive feedback, suggestions and encouragement throughout the project. I am grateful for the independence and productive work schedules through which I could deliver the best I could in this project. I want to thank my expert, Dr. Prasenjit Ghosh, for his comments and feedback. I sincerely cherish the friendly and inquisitive environment of the SAIMAT group at IISc, led by Sai sir. The excellent documentation of resources and concepts and the insightful discussions made my time at the group truly memorable. I would especially like to thank Reshma (a collaborator for one of my other projects), for guiding me through the lab's concepts and ideas, Jayant (for composition-space energy data), and the other members of the SAIMAT group. I want to thank Dr. Kaustubh Kaluskar and Dr. Sharan Shetty from Shell Markets Pvt Ltd, Bangalore who have been collaborators for one of my other projects during my tenure at the SAIMAT group. I want to thank Prof. Arun Venkatnathan for his valuable professional and personal advice and Prof. Arnab Mukherjee (and his group) who introduced me to my favourite topic of Computational Chemistry.

I acknowledge the Kishore Vaigyanik Protsahan Yojana – Inspire scholarship, DST, Government of India, for the fellowship. I am grateful to the computational resources provided by PARAM Pravega under the National Supercomputing Mission, Government of India, at the Indian Institute of Science and the Myriad Cluster computer at the University College, London which I have used to perform a few of my computations.

I thank my landlords Lalitha and Chandra paati, for the homely environment and hospitality they provided me during my stay near IISc for the MS thesis. Apart from research, I would like to thank all my friends who have made my life at IISER colourful. Words do not suffice to thank the Almighty, who, through my parents, has made me the person I am today.

Chapter 1 **Introduction**

1.1 The context

In the current society that we live in, with the increase in healthcare facilities and preventive medicine, the world population is increasing drastically. This increase in population demands facilities and resources to a larger extent than ever before. The transportation, procurement, manufacturing, disbursal and storage of these resources require enormous energy, as thermodynamic work is done on the systems involved in these processes. The conventional energy sources have been fossil fuels, which are practically non-renewable and are depleting with the increasing energy demand amidst geopolitical tensions. On the other hand, thermal power plants have excessive carbon dioxide, nitrogen oxides (NO_x), sulphur oxides (SO_x), and particulate matter emissions due to partial and inefficient combustion of coal to produce energy. These pollutants are greenhouse gases known to trap heat in the atmosphere, causing global warming, climate change, extreme weather events and eventually glacial melting [1]. The excessive presence of particulate matter makes the air unclean and causes allergies and infections in the respiratory tract.

These challenges call for renewable, green and alternative energy sources, described as follows: Renewable energy is obtained from naturally renewed sources within a human lifespan. Any energy source that is an alternative to fossil fuels is called an alternative energy source. A renewable energy source is considered to be green if it has minimal impact on the environment.

The Sun is a perennial source of energy as long as humanity lasts. It is the most suitable form of energy as a renewable and alternative source. If the method to harvest solar energy is efficient an makes a minimal environmental impact, it would also be a green energy source. The geopolitics of solar energy utilization would not be tense, as it can be harvested locally (in households, small buildings) and at a large scale (for industry and transport), based on its availability in the region. Since the Earth receives 2,00,000 times the world's electricity generating capacity daily [2], the optimal use, conversion and storage of solar energy would resolve the increasing energy demands and the associated tensions.

There have always been technologies which directly concentrate the Sunlight for daily use, like solar heaters, solar cookers, and solar lights; using it in a form which is convertible, storable and accessible would make the solar energy distribution and usage more efficient and versatile. Electricity is the form for apt storage, conversion to other sources and accessible (in various power scales and energy scales). Numerous technologies already implemented in society use electricity to power different processes at both the small scale (like households) and large scale (like electricity grids and transport). Therefore, a device that converts sunlight to electricity would bridge this gap. These are called photovoltaic (PV) devices or solar cells. PV devices directly convert sunlight to electricity without moving parts, emissions and sound, making them durable and robust [3].

1.2 The working of a solar cell

Solar cells are semiconductors that absorb light that is incident on them, create and dissociate the electron-hole pairs, conduct the electrons and holes (called carriers or charge carriers) and collect the carriers at the ends of the device. The input power density given by a light source to a solar cell is given by [3]

$$P_{in} = \phi\varepsilon$$

Equation 1

, where ε is the energy of the incident photon, and ϕ is the photon flux, given by the number of photons incident on the cell per area per unit time.

The charge carriers in solar cells are the electrons in the conduction band(s) and the holes in the valence band(s) due to photoexcitation. Different kinds of solar cells have been established, with their modifications to enhance solar cell performance. Here, we consider the single homojunction solar cell. This type consists of a p-type material (having higher carrier hole concentration or/and mobility, and a lower-energy fermi level) in contact with an n-type material (having higher carrier electron concentration or/and mobility, and a higher-energy fermi level), forming a p-n junction. The difference in fermi levels while the contact is made causes the diffusion current of electrons and holes, leading to an excess negative charge at the p-side and an excess positive charge at the n-side of the junction. This charge accumulates till the drift current due to the electrostatic potential caused by the excess charges balances the diffusion

current. The equilibrium charge distribution at the interface is called the depletion region, and the equilibrium electrostatic potential at the interface is called the built-in potential (V_{bi}). When light is absorbed by the solar cell, electrons are excited from the valence band to the conduction band, forming the exciton (the electron-hole pair), with the hole in the valence band. The exciton is dissociated with the built-in potential, causing minority carrier migration (electron in the p-side and hole in the n-side) and the charges are collected at the device's ends. The migration of the charges can also be understood as being due to the band-bending of the conduction and the valence bands near the depletion region due to static charges, and the carriers move according to the shape of the bent bands at the respective sides.

The built-in potential is caused due to the fermi-level difference that existed between the p and n-type regions before contact. If we assume that the same material is doped to make the p and n-type regions, both the regions will have similar (if not the same) placement of the valence band maxima (VBM) and conduction band minima (CBM). Since the fermi levels of both the regions are bound by the VBM and CBM, the difference between the CBM and VBM (i.e. the band gap E_g) can be the maximum value the built-in potential can take. This means that

$$V_{oc} \leq V_{bi} \leq E_g$$

Equation 2

, where V_{oc} is the open circuit voltage, the electrochemical potential difference between the device's ends when no net current flows.

The short circuit current density (J_{sc}) is the current across a solar cell when there is zero resistance in the load (external circuit) and without internal losses, per unit area of the device. The parameter that quantifies the performance of a solar cell is the power conversion efficiency for a solar cell is given by [3]

$$\eta = \frac{P_{output}}{P_{input}} = \frac{FF \cdot V_{oc} J_{sc}}{P_{input}}$$

Equation 3

, where FF is the fill factor of the device, which accounts for the losses in the internal circuit.

The higher the material's band gap, the lower the $J_{sc,}$ as only the photons of the solar spectrum having energies greater than the band gap are absorbed to create mobile electrons and holes constituting the current. This intuition calls for an optimum band gap of the material (1.4 eV), giving the maximum efficiency of 33%, called the Shockley-Queisser limit [4].

1.3 Silicon solar cells

The photovoltaics market began with commercializing silicon solar cells, mainly due to their abundance in the Earth's crust. It has a commercial efficiency of about 22% [9] for the single-junction versions. Its indirect band gap of about 1.12 eV, despite falling in the range of 1.1 to 1.5 eV, is not considered suitable since it confers poor optical absorption due to the forbidden band gap transitions. This property requires that thick sheets (200-500 μm) [3] of silicon are needed to prepare the solar cell for a given absorption of sunlight (and therefore, current generated), which increases its manufacturing and installation costs [6, 7]. The photons of energies beyond the band gap are absorbed, but the electrons tend to thermalize to the CBM (and holes to VBM), leading to thermal losses in the system.

Crystalline silicon of extremely high purity is required to prepare the solar cells, which is also a reason for the high manufacturing costs. It is metallurgically obtained by heating silica (SiO_2) in coal furnaces to about (1500-2000 ^oC) to form metallurgy grade (98% pure) silicon, along with releasing a stoichiometric amount of carbon dioxide [3, 8], which adds to the fact that the procurement process is not green. Metallurgy-grade silicon must be further refined to solar-grade silicon (single crystal or multi crystalline silicon), as silicon solar cells are extremely sensitive to impurities [9]. The purity of silicon is measured by the 'N' number, where N denotes the number of significant digits of 9 after the decimal in 99% purity. For example, 7N silicon refers to 99.9999999% pure silicon. Typically, at least 3N pure silicon is required for photovoltaic applications, which is achieved through complex chemical separation methodologies [1]. Silicon is also brittle, which requires precise equipment to be used for its handling and manufacturing. Despite the efforts to tackle these disadvantages of silicon, the single junction solar cell has almost saturated in its efficiency and performance, making us look out for other materials for photovoltaic applications.

1.4 Beyond-Si photovoltaics

Beyond-Si photovoltaics are other materials that could be used as an alternative to silicon and are expected to perform better than silicon for photovoltaic applications. In this study, since we evaluate the performance of materials based on their ability to be prospective homojunction solar cell materials, we impose the same constraint on the definition of beyond-Si photovoltaics. In order to perform equal to or better than silicon, certain characteristics must be satisfied by the beyond-Si photovoltaic material considered, which are described henceforth.

The material must be non-toxic, and the elements present in the composition must also be non-toxic. This means that the material must not be toxic to any organisms (including humans) at any stage of its preparation and disposal after use. The process for procurement, manufacturing and disposal of the material in its purest state (as required for PV applications) must be green. We assume that this criterion is automatically fulfilled if the elements present in the ceramic material are naturally abundant in the same oxidation state as in the material since minimal input of energy and other components would be required to prepare the material.

The material must be stable at the temperature at which it is prepared, characterized and used. It must be resistant to the components of the atmosphere (like water, oxygen and other gases). The material must not decompose to sublimate into volatile products or transform its phase during the working period. It must have long-term stability and must output similar efficiency throughout its lifetime. Additionally, the material should have reasonably high toughness. Few mobile PV applications demand that the materials must be flexible. PV cells used in astronomical applications must be stable under low or minimal air pressures and a wide range of temperatures.

Most importantly, the material must have a direct band gap (or nearest direct band gap) of around 1.4 eV to achieve an efficiency close to the Shockley-Queisser limit [4]. Few studies [6, 7] consider the range of 1.1 to 1.5 eV for the band gap, while others consider higher upper bounds [11]. These limits are subject to the spectrum of light under which the PV device is meant to work. Additionally, doping the materials might change the material's band structure, and hence the band gap. Therefore, the band gaps must follow the same criteria after doping [12, 13]. The charge carrier mobility,

and hence the lifetime (resistant to carrier recombination) must be high to collect enough carriers at the ends of the solar cell to generate current. The higher the current collected per input power, the higher the efficiency. These properties also depend on the dopant concentration and must be fulfilled after doping [13, 14]. The material must not be reflective in the solar spectrum range; it must have an appreciable solar adsorption coefficient [15].

The material must be resistant towards forming intrinsic defects and must allow doping. While the feasibility of doping the material is a property of the dopant, the material's structure and composition dictate its resistance towards forming intrinsic defects. The defects play as (deep) trap states for the charge carriers, reducing the charge collection at the device's ends, per unit of input power. Few defects act as resistances that hinder the flow of charge across them. This results in losses of the potential used to drive them, ultimately reducing the net output power of the solar cell. Defects also change the band structure of the solid, which is unfavourable unless they are intentionally created or predicted [16].

1.5 Previous studies on beyond-Si PVs

Like any other materials discovery or design problem, the discovery and optimization of beyond-Si PVs involves the collaboration and feedback between data science, computational and experimental studies. In the recent upsurge of artificial intelligence and relatively free access to previously studied experimental and computational data, there have been many machine-learning-based screening and property prediction of solar cell materials, as well as studies that optimize the performance of solar cells [17, 18].

While the data from machine learning may not be completely accurate, they may be useful for filtering out prospective materials within a certain error range. Ab-initio thermodynamics and electronic structure-based computations have been done to validate these materials' prospects further. Several unit cell-level properties like thermodynamic, electronic and optical properties have been computationally studied [6, 7, 12, 19]. There have also been numerical models to simulate the charge carrier generation, migration, recombination and collection processes in opto-electronically active materials [20].

The materials which have been predicted to be hopeful by simulations have been experimentally validated and verified using synthetic protocols to synthesize the materials and characterize them using techniques like single-crystal X-ray diffraction (XRD), Angle Resolved Photo Electron Spectroscopy (ARPES) and Cyclic voltammetry [21, 22]. Further, interface-level studies have been done to tune the electronic properties with the help of appropriate doping. The device-level efficiency is maximized by bulk synthesis of the material(s), along with modifying parameters like the area exposed to light, the relative thickness of the n and p sides, and adding extra layers like the anti-reflective coatings [23]. This workflow of using data, computations and experiments sequentially has proven useful for discovering new solar cell materials.

Various classes of materials have been explored previously for their ability to be successful beyond Si PV candidates. Bulk ceramic materials like halide perovskites and chalcogenides have displayed suitable band gaps for PV applications [24]. A few studies have been done to tackle the air instability of halide perovskites [25]. Among chalcogenides, transition metal (non-redox-active) dichalcogenides like MoS_2 have been well studied [26]. Copper zinc tin sulphide (CZTS) in its twin polymorphs, kesterite and stannite, has been established computationally and experimentally as a thin film solar cell material [12, 27]. Silicon carbides and germanium carbides have been studied for photovoltaic effects.

Various classes of 2D materials, like nanosheets, have been established as prospective photovoltaic materials [28]. MXenes have increased in popularity for PV studies due to the flexibility of adding multiple types of layers that differ in electronic properties [29]. Other nanomaterials like quantum dots have been explored because of unique band structures that develop based on the size of these materials [30].

Organic-Inorganic hybrid materials like perovskites have been extensively studied for their optoelectronic and structural properties [31]. Organic photovoltaics consisting of polymers tend to be biodegradable and require milder conditions to synthesize. Particularly, polycyclic aromatic compounds of different functional groups show different electronic properties like the HOMO and LUMO levels, which alter the band gap of the material according to its utility [32].

1.6 Pnictides – an overview

Pnictides are ceramic compounds with Group-15 elements (pnictogens) having a -3 oxidation state. Gallium arsenide (GaAs) (Ga in +3 oxidation state and As is -3 oxidation state) is a well-studied pnictide for photovoltaic applications and is fabricated and optimized at the device-level [23]. However, the presence of arsenic in GaAs makes it toxic during disposal, which could hence be a threat to the environment. Antimony and bismuth do not show a stable -3 oxidation state due to their lower electronegativity. They tend to show metallic behaviour and prefer higher oxidation states. In addition to being toxic, this aspect of bismuth makes Bi^{3-} compounds less preferrable, despite the numerous studies on boron antimonide (BSb), indium antimonide (InSb) and gallium antimonide (GaSb) solar cells [34, 35, 36]. BN tends to show hot carrier transport capabilities, which means that the carriers excited beyond CBM (VBM if hole) do not thermalize to the CBM and retain the kinetic energy, increasing the device's output power due to lesser thermalization losses.

Previous studies on mono (binary) pnictides have suggested their prospect of being used as candidate photovoltaic materials [7, 33]. Nitrides have been understood as having optimal band gaps due to the matching (slightly lower) electronegativity with Group-13 elements like gallium [37]. Additionally, they are known to be chemically stable at high temperatures. The first-principles study in [7] has established that among binary A_3B_2, ternary $AA'B_2$ and a quaternary $AA'A''B_2$ (A = Sr, Zn, Ca and B = P or N); $SrZn_2N_2$, $SrZn_2P_2$ and $CaZn_2N_2$ can be promising beyond-Si PV candidates. Thay have also identified that $ZnCa_2N_2$ and $ZnSr_2N_2$ may be prone to form nitrogen vacancies.

Compounds of the ABX (A = Li, Na, K; B = Ca, Zn; D = Al, Ga, In; X= N, P) class have been explored for their optoelectronic properties [38]. Similarly, the BDX_2 class of compounds have also been studied before. Studies have been conducted on the electronic structures of K_4ZnP_2 and K_4CdP_2, hinting their utility in PV applications [39].

However, no computational study in the literature considers the broad chemical space of Group 1, 2 and 13 binary, ternary quaternary pnictides together to evaluate their properties and identify them as photovoltaic candidates. Moreover, many compounds of this chemical space have previously been unexplored computationally or experimentally for their structural and electronic properties. We lack information about

electronic and thermodynamic properties for the compounds whose structure is known in relevant chemical databases, which would be relevant for PV applications.

The above argument is the motivation of this study to do high-throughput screening and calculations based on ab-initio methods to explore the large chemical space of pnictides and evaluate their potential of being candidate photovoltaics materials which could be taken up for further experimental studies to validate and optimize their performance in the future. We hope this thesis will be useful for experimental studies on pnictides or computational studies of other chemical spaces. Each subsection of Chapter 2 (from 2.2) refers to a calculation/consideration determining a property of each composition, where certain criteria are expected to be satisfied by each candidate. If the respective criteria are satisfied by a candidate, it is considered for the next calculation. Else, it is neglected.

Chapter 2 **Theory and Methods**

This chapter describes the theory of the procedures used in the thesis, their specifics and implementation.

2.1 Computational methods

We use computational methods to solve for the wave functions of the electrons in the system using quantum mechanical theories and approximations to study the material's properties. Under the Born-Oppenheimer approximation, the electronic wavefunction of the system is decoupled from the nuclear wavefunction and hence is solved with various electronic structure theories. Throughout the thesis, structural relaxations, electronic structure calculations and the calculation of thermodynamic properties were done using Density Functional Theory (DFT) [40] as implemented in the Vienna Ab initio Simulation Package (VASP) [41]. The formalism of the DFT is briefly described as follows;

The Hohenberg-Kohn theorem states that the total energy of a many-electron system in the ground state is uniquely defined by the electron density (n). It turns out that the ground-state electron density (n_0) minimizes the total energy, $E = F[n]$. This Hohenberg-Kohn Variational principle [42] leads to the construction of single-electron orthonormal wave functions (KS orbitals) $\varphi_i(r)$ which follow the Kohn-Sham equations [40];

$$\left[-\frac{1}{2}\nabla^2 + V_{tot}(r)\right]\varphi_i(r) = \varepsilon_i\varphi_i(r)$$

$$V_{tot}(r) = V_n(r) + V_H(r) + V_{xc}(r)$$

$$V_n(r) = -\sum_I \frac{Z_I}{|r - R_I|}$$

$$\nabla^2 V_H(r) = -4\pi n(r)$$

$$V_{xc}(r) = \frac{\partial E_{xc}[n(r)]}{\partial n}$$

$$n(r) = \sum_i |\varphi_i(r)|^2$$

Equations 4

Where *i* indices over the electrons and *I* indices over the nuclei, *r* is the set of coordinates (x,y,z). V_n denotes the external or nuclear electrostatic potential faced by an electron. V_H is the Hartree potential that accounts for the mean-field potential in the presence of other electrons in the vicinity, which act as charge clouds. V_{xc} is the exchange-correlation (XC) potential considered for solving the system. These equations can be solved iteratively by initially guessing for an electron density, computing the Hartree potential, approximating the XC potential, solving for the single-electron wave functions (using discretization of space and diagonalization procedures), and arriving at the electron density. If the derived density matches the energy due to the guessed electron density within the bounds of a given energy cutoff, it is returned (termed as electronic convergence). Else, the derived density is used in the first step until the convergence is reached. This cycle is called the self-consistency field method (SCF) to arrive at the electronic properties and the energy eigenvalues (ε_i), given a nuclear configuration ($\{R_I\}$).

The XC functional signifies the effect of the exchange interactions (a result of the orthonormality of the orbitals and Pauli's exclusion principle) along with the quantum correlation of other electrons with the considered orbital. These are usually approximated by considering the electrons as an inhomogeneous electron gas. Except for the band structure calculations, the Strongly Constrained and Appropriately Normed (SCAN) XC functional is used to approximate the XC energy [43]. It is a nonempirical semi-local meta-Generalized Gradient Approximated (meta-GGA) functional. Meta-GGA functionals have spin-density gradients and orbital kinetic energy densities added to the GGA framework, where the XC energy is approximated as a functional of the electron density and its gradient. They recognize covalent single, metallic and weak bonds through their construction, and are known to predict polymorph stability better. Previous studies have used the SCAN functional to evaluate the structural properties of chalcogenides and pnictides [7, 44].

Typically, the functional form of the orbitals is expanded into linear combinations of basis functions, which form the basis set. The problem of arriving at the orbitals during the SCF reduces to finding the coefficients of the basis functions in each orbital. In VASP, like other software for solving condensed matter systems with periodic boundary conditions, the plane wave basis set expands the orbitals. By virtue of the Bloch theorem, each KS orbital can be written as [45]

$$\varphi_{ik}(r) = u_{ik}(r)e^{ik.r}, \text{ and}$$

$$u_{ik}(r) = \frac{1}{\sqrt{\Omega}}\sum_{G} C_{Gik}e^{iG.r}$$

Equation 5

Where k is the crystal momentum which is in the reciprocal space, and can be proven to be within the first Brillouin zone of the crystal and are called the k-points of the Brillouin zone. Ω is the volume of the primitive cell of the crystal in real space. G are the reciprocal lattice vectors that span all lattice points in the crystal. In principle, G can span all the lattice points in the whole bulk of the crystal. For ease of computation, an Energy cutoff (E_{cut}) [45] is defined, where the basis set includes all plane waves indexed by G for which

$$\frac{\hbar^2}{2}|G + k|^2 \leq E_{cut}$$

Equation 6

Therefore, the value of E_{cut} determines the number of unit cells in the reciprocal space considered for the constructions of the plane-waves.

Ideally, infinite numbers of k values have to be considered in the first Brillouin zone to describe the periodic replica of the unit cell. For the SCF calculation (except for band structure), the k-points are evenly spaced in a regular mesh in the first Brillouin zone. The evenly spaced mesh ensures that Brillouin zone sampling is systematic and unbiased, and the overall electronic properties of the material is captured. For the band structure calculation, a k-path with specific high-symmetry k-points is sampled, as discussed in Section 2.5. The study in [7] used a k-point density of 32 k-points per angstrom. In order to choose the k-point density in the reciprocal lattice and check if higher k-point densities are required, we have considered the total energies of $CaSrZnP_2$ with 32 and 48 k-points per angstrom. Since the difference in total energies with 32 and 48 k-points per angstrom is less than 0.1 meV/atom (the typical numerical error that occurs with DFT), we proceed to use a k-point density of 32 k-points per angstrom for all the structural relaxations for faster convergence. The k-mesh constructed is centred at the gamma point, which is the origin of the Brillouin zone.

Throughout the thesis, an energy cutoff of 520 eV has been used to truncate the basis set. In order to choose this value, the total energy of a specific crystal is considered with increasing plane wave cutoff energies. The energy cutoff for which the value of

the system's total energy does not differ much from that with the next higher energy cutoff chosen for studying the system. The studies in [7] have reported the convergence of pnictide total energies at this value, leading us to consider the same value for the thesis.

Throughout the thesis, we perform spin-polarized calculations for the SCF, treating the spin-up and spin-down states as distinct. The spin-dependant effective potentials are used in the Kohn-Sham equations, and the Kohn-Sham orbitals are hence spin-dependant [45].

To construct pseudopotentials, VASP uses the Projector Augmented Wave (PAW) method [45, 46]. For periodic systems, many plane waves are required to describe the oscillations (due to nodes) of the orbitals near the nuclei. The PAW method redefines orbitals to be identical to the true wavefunctions outside a given cutoff radius around a nucleus and are smooth approximations of the true orbitals inside the cutoff radius. These calculations were done for isolated atoms of each element, and the values of the pseudo-orbital coefficients are written in each pseudopotential file, as given in VASP. A frozen-core approximation is considered in PAW, which considers only the valence electrons of each atom to contribute to the physical and chemical properties of the system and that the core electrons screen the nuclear potential such that the valence electrons experience an effective potential due to the core electrons and the nucleus. For each atom type, many pseudopotentials are available, based on the number of valence electrons considered, the cutoff radius for the PAW method, and the XC potential used. For the elements chosen involved in this thesis, the following pseudopotential descriptions available in VASP are chosen as given in Table 1;

Table 1: The pseudopotential files of VASP chosen for each element, with the valence electrons considered and the outermost cutoff radius for pseudization procedure

Element	Pseudopotential name	Valence electrons	Outermost cutoff radius (angstrom)
Calcium	Ca_sv 06Sep2000	3s, 3p and 4s	2.3
Strontium	Sr_sv 07Sep2000	4s, 4p and 5s	2.5
Zinc	Zn 06Sep2000	3d and 4s	2.3
Magnesium	Mg_pv 13Apr2007	2p and 3s	2.0
Nitrogen	N 08Apr2002	2s and 2p	1.5
Phosphorus	P 06Sep2000	3s and 3p	1.9
Lithium	Li 17Jan2003	2s	2.05
Sodium	Na_pv 19Sep2006	2p and 3s	2.2
Potassium	K_sv 06 Sep2000	3s, 3p and 4s	2.3
Aluminium	Al 04Jan2001	3s and 3p	1.9

Gallium	Ga_d 06Jul2010	3d, 4s and 4p	2.5
Indium	In_d 06Sep2000	4d, 5s and 5p	2.5

Except for Indium and Gallium, these are chosen based on the findings of previous studies [7]. In order to choose between *Ga* (having 4s and 4p valence electrons) and *Ga_d* pseudopotentials for gallium and between *In* (having 5s and 5p valence electrons) and *In_d* for Indium, we use both types of potentials to calculate the formation energy of experimentally known gallium sulphides (GaS and Ga_2S_3), gallium phosphide (GaP) and indium phosphide (InP). Since the energies of the considered compounds using *Ga_d* and *In_d* pseudopotentials for gallium and indium, respectively, are more similar (than the values obtained with *Ga* and *In* pseudopotentials) to their corresponding experimentally determined formation enthalpy values, *Ga_d* and *In_d* are used as pseudopotentials for gallium and indium respectively.

In VASP, smearing and partial occupancies decrease the number of k-points required to calculate an accurate electronic structure and electron density. The total energy of a system over filled parts of bands would be [45]

$$\sum_i \frac{1}{\Omega_{BZ}} \int_{\Omega_{BZ}} \varepsilon_{ik} \Theta(\varepsilon_{ik} - \varepsilon_F) dk$$

Discretization of the Brillouin zone into k-points transforms this integral to $\sum_k w_k \, \varepsilon_{ik} \Theta(\varepsilon_{ik} - \varepsilon_F)$ where Θ is the Dirac step function, w_k are the weights associated with the k points (of similar symmetries) and ε_F is the fermi level. The step function (and occupancies) jumps (jump) from 1 to 0 at the fermi level, which causes convergence issues. Therefore, Θ is replaced by a smooth function $f_\sigma(\{\varepsilon_{ik}\})$ where σ is the width of smearing. Throughout this thesis, except for density of states calculations, a Gaussian smearing function is used with σ set as 0.05 eV. Gaussian smearing is described as [45]

$$f_\sigma(\varepsilon) = \frac{1}{2}(1 - \mathrm{erf}\left[\frac{\varepsilon - \varepsilon_F}{\sigma}\right])$$

Equation 7

2.2 Structures considered and relaxed

For the thesis, we search popular databases like ICSD [47], Materials Project [48], OQMD [49], Nomad [50] and Google scholar to look for pnictide compounds with the following sets of elements and their valencies:

X^{3-} = N, P

A^{+} = Li, Na, K

B^{2+} = Mg, Ca, Sr, Zn

C^{3+} = Al, Ga, In

D^{4+} = Si, Ge, Ti, Sn, Pb

These elements are chosen as they are abundant and cheap, non-toxic and redox inactive (less prone to decomposition and oxidation in the presence of air), as discussed in the Introduction chapter. With these elements, based on allowed stoichiometries for maintaining charge neutrality with their given oxidation states, we list compound classes. The compound classes listed are ABX, B_3XX' (where ‘ and “ represent those non-identical elements from the X set), D_3X_4, A_3X, $CC'X_2$, $ABCX_2$, BDX_2, A_2DX_2, A_4BX_2 and $BB'B''X_2$. In theory, more classes can be listed, but we list these due to the availability of time for scanning. We permute all the elements of each set in each class to have a list of possible compounds for each class. We search all the databases for the experimental synthesizability, their band gap and previous claims and proposals of being used as alternative photovoltaic materials. Among the listed classes, we choose the $ABCX_2$, $A4BX_2$ and $BB'B''X_2$ classes of compounds for our study, since the compounds of the other classes have either been well-studied and established before or do not have any experimentally or computationally observed structures in either of the databases. Additionally, a few compounds of the three classes considered have optimal band gaps which are either experimentally observed or computationally calculated. 3*4*3*2 = 72 compositions are considered for the $ABCX_2$ class, 3*4*2 = 24 compositions are considered for the $A4BX_2$ class and $\binom{4}{3}$*2 = 8 compositions are considered for the $BB'B''X_2$ class, including their respective templates.

In order to initialize crystal structures for the compositions in the A_4BX_2 class, we consider the experimentally observed crystal structures of K_4ZnP_2 (R-3mH space group, ICSD coll. Code 67261) and Li_4SrN_2 ($I4_1/amd$ space group, ICSD coll. Code 87413) as the templates for the theoretically derived structures of all the compositions

considered in the A_4BX_2 class. The primitive unit cell of Li_4SrN_2 is considered for initializing the structures for quicker calculations compared to those with using the tetragonal conventional cell. For initializing the structures of the compositions of $ABCX_2$, we consider the observed crystal structures of $LiCaGaN_2$ ($P2_1/c$ space group, ICSD coll. code 424911) and $LiSrGaN_2$ (C2/m space group, ICSD coll. Code 96224).

For initializing structures of the $BB'BX_2$, we do not find any experimentally observed structure for compounds belonging to this class; hence, we consider the theoretical structures postulated by previous studies on the same class of compounds [7]. The templates considered are $CaSrZnN_2$ with the $ZnSr_2N_2$-derived I4/mmm structure and $CaSrZnP_2$ with the $CaZn_2P_2$-derived P-3m1 structure, which were found to be the stable polymorphs for their corresponding compositions. With the templates for each class of compounds, the structures of each composition in a class according to both the templates for each class are obtained by substituting the sites of the template with the corresponding element of the same oxidation state as to the initial occupant of the site. For example, to derive the R-3mH structure of Li_4ZnN_2, all the K^+ are replaced by Li^+, and P^{3-} replaced by N^{3-}, and the Zn atoms are left as they are. The structures of the templates are given in Tables 2, 3 and 4.

In order to confirm that these are the possible structures for the respective class of compositions, we consider the experimentally observed structures of other compositions like K_4CdP_2, Na_4CdP_2, $LiCaAlN_2$. Since these compositions also have the same structures as initialized, we proceed to consider only two possible structures for a composition in each class.

Table 2: The structures of K_4ZnP_2 (left) and the primitive cell of Li_4SrN_2 (right) used as the templates for initializing the structures for each of the compositions of the A_4BX_2 class. In the three tables below, the a, b, c axes are marked at the left of each structure. The colours of the atoms denote the following elements; light purple for K, grey for Zn, red for P, blue for Li, green for Sr, white for N, yellow for Ca, and dark violet for Ga.

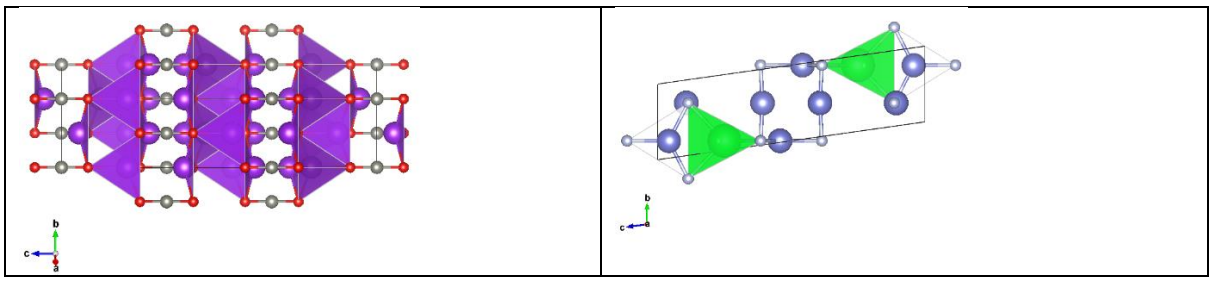

Table 3: The structures of $LiCaGaN_2$ (left) and $LiSrGaN_2$ (right) used as the templates for initializing the structures for each of the compositions of the $ABCX_2$ class.

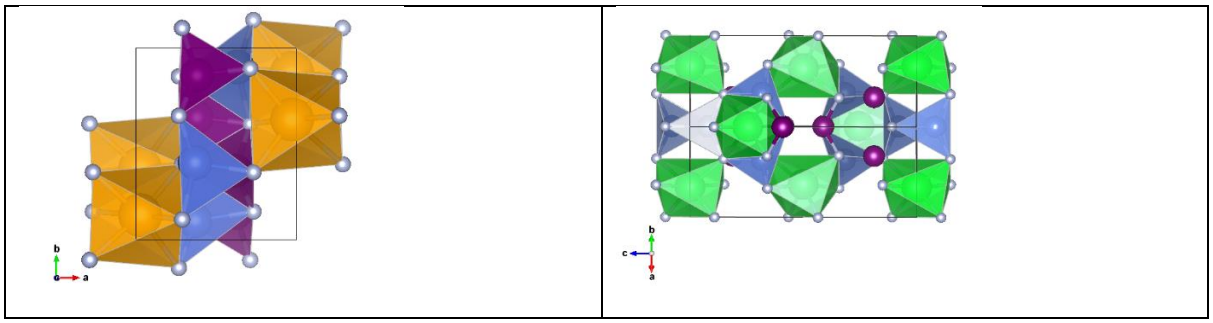

Table 4: The structures of $CaSrZnP_2$ (left) and $CaSrZnN_2$ (right) used as the templates for initializing the structures for each of the compositions of the $BB'B''X_2$ class.

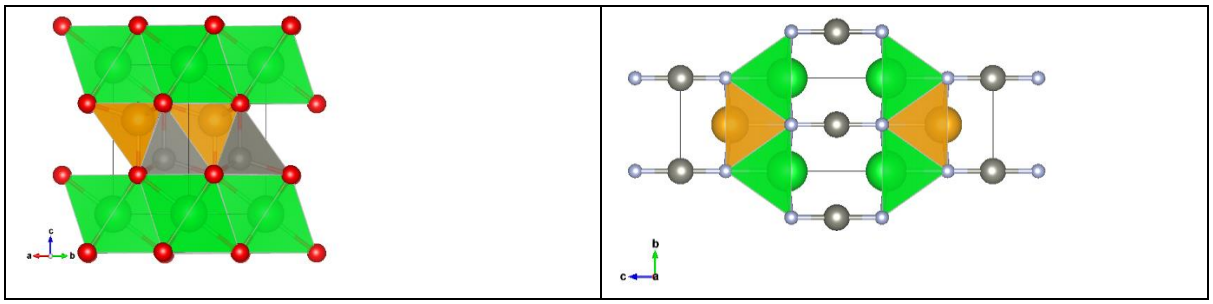

2.3 Structure relaxation and Thermodynamic stability

In each class, each composition has two structures in which it is initialized. Despite the similarity of the occupants of each structure compared to the parent structure (template), the difference in electronegativities and atomic radii of each atom at a site compared to the atom in the parent structure, we perform structural relaxation of each structure of a given composition.

We use the Conjugate Gradient algorithm as implemented by VASP [45] for structural relaxation. Given a configuration, the derivative of the total energy with respect to the atomic coordinates of each atom gives the forces on each atom. The initial search (displacement) direction for each atom is chosen along the line of forces, with the next search direction being mandated to be perpendicular to the initial direction. A trial step is performed into the search direction and the energies (with an SCF cycle), forces and stresses are recomputed. A polynomial is fitted to determine the minimum expected energy based on the recomputed energies and forces compared to those of the previous step. If the forces and stresses along the search direction vanish after this step, the next trial step is performed. Otherwise, further steps are performed in the same search direction. The above cycle repeats until all the components of forces on

each atom are less than a given force cutoff value. For the structural relaxations in this thesis, we set the force cutoff to 0.01 eV per angstrom.

After both the structures (polymorphs) for each composition have structurally relaxed, we consider the total DFT-calculated energy per formula unit of each polymorph. The polymorph with a lower DFT-calculated energy per formula unit is considered as the ground state (relatively more stable) polymorph. For each composition, we consider only the ground state polymorph for further analysis and calculations. This consideration is justified below.

Like any chemical system considered, for solids like pnictides, assuming they are closed systems (do not allow mass transfer with surrounding) many processes are performed at a constant pressure (usually the atmospheric pressure), temperature and number of moles. Therefore, in order to study the thermodynamic feasibility of a process, the Gibbs free energy (*G*) of the system must be considered as the thermodynamic potential. A process (a reaction r in our case) is considered feasible if the *G* of the system reduces as the process is performed, going from the initial (i) to final (f) state of the system. Here, we assume all extensive thermodynamic quantities are to be per formula unit of the system. Mathematically, $\Delta_r G = G_f - G_i < 0$ for a thermodynamically feasible reaction. For a state of the system, its Gibbs free energy is

$$G = U - TS + pV$$

Equation 8

Where *U* is the internal energy (in our case, the DFT-calculated energy) per formula unit, *T* is the absolute temperature, *p* is the pressure applied on the system and *V* is the volume per formula unit of the system. Since we consider the process happening at 0 K as we ignore the excited states, the *TS* term vanishes. The *pV* term is negligible compared to *U*, considering the volume of a formula unit and the atmospheric pressure. Hence, we see that $G \approx U$ for closed solid systems consisting of a single (few) unit cell(s). Therefore, we use the *U* (or DFT-calculated energy per formula unit) as the thermodynamic potential here. It is thus justified the process where a polymorph with lower DFT-calculated energy per formula unit transforms to a polymorph with higher DFT-calculated energy per formula unit is thermodynamically unfeasible, and the polymorph with lower DFT-calculated energy per formula unit is relatively stable.

A material must not decompose into other components as a PV device. In order to verify the thermodynamic infeasibility of each relatively stable polymorph for a composition converting/decomposing to other compounds in their respective chemical space, we construct the thermodynamic phase diagram (at 0 K temperature) of the chemical space of each polymorph. The formation energy of compound $X_xY_yZ_z$ (in the chemical space of elements X, Y, Z) is defined as [51]

$$\Delta E_f\left(X_xY_yZ_z\right) = E\left(X_xY_yZ_z\right) - xE(X) - yE(Y) - zE(Z)$$

Equation 9

Where $E(X_xY_yZ_z)$ is taken as the DFT energy per formula unit of the compound and E(X), E(Y) and E(Z) are energies per atom of the elements X, Y, Z in their respective bulk phases. Positive ΔE_f values indicate that the compound is unstable relative to the elements. Any compound in the X-Y-Z chemical space can be written as $X_uY_vZ_{1-u-v}$ where *u* and *v* range from 0 to 1 and parametrically represent and span the chemical space. Now, the convex hull of stability is the lower convex envelope that joins the points in the ΔE_f v/s {u, v} space. The convex hull can be roughly thought of the curve through the set of extreme points that bound the set. However, we do not concern ourselves with the upper convex hull of the space (having $\Delta E_f > 0$) as the compounds represented by the points are unstable.

It can be proven mathematically that a compound is said to be thermodynamically stable against decomposition and phase transformation (already considered while only including the relatively stable polymorph) if and only if it lies on the convex hull of stability in the corresponding chemical space. Else (lies above the convex hull), it is thermodynamically unstable. The vertical distance of the point in the ΔE_f v/s {u, v} space representing a compound from the convex hull is termed as the energy above hull (E_{hull}), which is always greater than or equal to 0. It represents the degree of instability of the compound. This concept explained with three elements in the chemical space can be extended to two or more elements.

For binary (two elements) chemical spaces, the convex hull is plotted with ΔE_f in the Y-axis and relative fraction of an element (like u) in the X-axis. For ternary (three elements) chemical spaces, ΔE_f is plotted on the Z-axis, with an equilateral triangle in the X-Y plane whose vertices denote the pure element, and the 3-D convex hull is constructed. A projection of this 3-D convex hull on the equilateral triangle is taken

with the stable phases denoted as points and connected by lines. These lines are called the tie-lines and the triangles enclosed by the tie-lines are called Gibbs triangles. For a quaternary (four elements) chemical space, the projection of the 4-D convex hull is considered on the 3-D regular tetrahedron with vertices representing pure elements. Here, the tie-lines enclose the Gibbs tetrahedra. Any compound on (not below) the tie-line is in chemical equilibrium with the compounds that connect the tie line.

There exist compounds known as metastable phases, which are thermodynamically unstable, but are kinetically trapped in a local minimum of the Energy v/s state-space curve. A famous example of a metastable phase of carbon is diamond, which is observed at room temperature and pressure, and does not readily decompose to graphite at NTP. This is because diamonds, being a stable phase at higher pressures, are formed at higher pressures. Nevertheless, its transformation to graphite, although thermodynamically favourable at room temperature, is kinetically very slow. Hence, the diamond allotrope is observed at NTP and has been used by humans for many centuries without decomposition.

For each ground-state polymorph of a composition in each class, we construct the convex hull of stability in the chemical space in which it belongs. To construct it, we search the ICSD [47] database for all the experimentally observed compounds (including their own polymorphs) in each chemical space and the elements in the chemical space. We call these subsidiary compounds. These structures of the subsidiary compounds and the elements are structurally relaxed using an equivalent set of DFT input parameters as for the candidates considered, to obtain their DFT energy per formula unit. These values and the candidate's DFT energy per formula unit (ground state polymorph) are used to calculate the 0K convex hull of the respective chemical space, using the pymatgen.analysis.phase_diagram.PhaseDiagram class of the Pymatgen module [64] in Python. If the candidate compound is on the convex hull, it is stable with respect to decomposition into other components (subsidiary compounds or elements) of the chemical space (with the same average composition) and is hence considered for further calculations.

Since there are many metastable compounds that are synthesized and used, we also consider the metastable compounds for further calculations, assuming that there can be methods or conditions developed to arrest them at room temperature and pressure. Previous studies have shown the correlation of metastability of the compound with its E_{hull} [53]. The studies conclude that the threshold value for E_{hull} under which a compound can be considered metastable is specific to the chemical family of the compound. Although they have shown that pnictides having E_{hull} values below 100 meV/atom tend to be metastable, we impose a stricter upper bound of 30 meV/atom to be the maximum E_{hull} for which a compound is considered metastable since compounds with higher values of E_{hull} are susceptible to form point defects [7].

For example, consider the stable polymorph of K_4SrP_2 composition for constructing the convex hull in the K-Sr-P chemical space. The structures of all experimentally known compounds in the chemical space viz. elemental K (stabler polymorph as found by DFT), Sr and P along with Sr_3P_2, SrP, Sr_3P_4, SrP_2, SrP_3, Sr_3P_{14}, KP, K_3P, K_4P_3, K_4P_6 are relaxed with similar input DFT parameters as for K_4SrP_2. Their DFT-predicted energy per formula unit is considered and input into the pymatgen code which constructs the convex hull as shown in Figure 1.

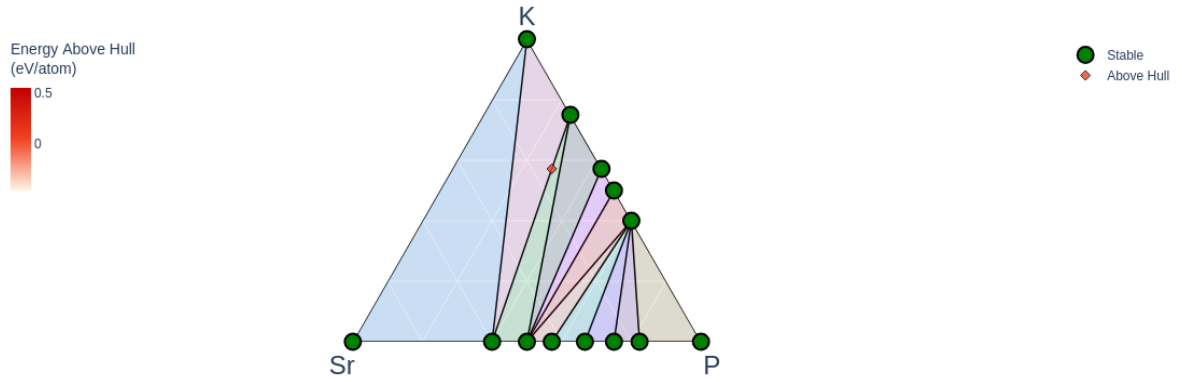

Figure 1: The 2D projection of the ternary convex hull of the K-Sr-P chemical space, with green dots representing points on the convex hull, and the red dot representing K_4SrP_2 which lies above the hull. The triangles shown in different colours are the Gibbs triangles, bound by tie-lines that connect the stable points.

2.4 Density of States Calculation

Electrons in solids form bands. Each electron occupies discrete orbitals in isolated atoms like 2s, 2p, 3d, etc. The core electron levels remain unperturbed due to their strong interaction with the respective nuclei when they are condensed to form a solid.

However, the valence electrons interact with each other and form closely spaced discrete states so numerous that they are almost indistinguishable and form a continuum called bands. The density of (electronic) states (DOS) is defined as the number of electronic states per unit energy. For a free electron (having no potential energy) in one-dimension [54], the energy

$$\varepsilon_k = \frac{\hbar^2}{2m} k^2$$

Equation 10

Where k is the wave vector of the electron and m is its mass. The total number of states (ζ) having energy ε is

$$\zeta = \frac{V}{3\pi^2} k^3 = \frac{V}{3\pi^2} \left(\frac{2m\varepsilon}{\hbar^2}\right)^{3/2}$$

Equation 11

The density of states D(ε) is

$$D(\varepsilon) = \frac{d\zeta}{d\varepsilon} \propto \varepsilon^{1/2}$$

Equation 12

This concave curve represents the maximum density of states any solid can have. At non-zero temperatures, the probability of electronic occupations of these states is given by the Fermi-Dirac distribution,

$$f(\varepsilon) = \frac{1}{1 + e^{\frac{\varepsilon - \varepsilon_F}{k_B T}}}$$

Equation 13

Where k_B is the Boltzmann constant, ε_F is the Fermi level and T is the absolute temperature. At 0 K, all states below the fermi level are completely occupied and those above the fermi level are completely unoccupied. In the case of a semiconductor (or insulator), the presence of the weak periodic potential causes the electrons to diffract at the Brillouin zone edges, causing a band gap (E_g). This phenomenon splits the electronic energy bands into valence bands (fully occupied at 0 K) and conduction bands (completely unoccupied at 0 K), with the Fermi level placed above the valence band energies and below the conduction band energies.

The presence of periodic potentials alters the shape and characteristics of the DOS versus energy plot (DOS plot), consisting of maxima and minima representing large and small numbers of electronic states at the respective energies. The nature of the DOS plot gives information about the electronic properties of a compound, i.e. if the Fermi level has any electronic states, the system is metallic (lacks a band gap); else, it is a semiconductor or an insulator. For semiconductors or insulators, the energy gap between the lowest available state above the Fermi level (the CBM) and the highest available state below the Fermi level (the VBM) is the band gap, which is of utmost importance for photovoltaic materials, as discussed earlier.

The projections of the total density of states into individual contributions from each orbital of all the atoms present in the system prove useful to qualitatively understand the bonding strength and the electronegativity differences of the atoms in the solid. Suppose two orbitals from different atoms have similar shapes of the projected DOS at the same energy. In that case, it means that they have aligned energies and hence, strongly interact to form new (bonding and antibonding) states indicative of a covalent bond with significant delocalization of the electron density into both atoms.

In order to check for the band gap of the stable (or metastable) candidates from each class, we perform density of states calculations for each of them. We perform an SCF calculation in VASP with an SCF energy cutoff of 10^{-6} eV. For higher precision of k-point sampling, we sample the first Brillouin zone with a k-point density of 96 k-points per angstrom. The higher value is important to ensure that fewer states between adjacent k-points are missed during the calculations. We consider the energies from -20 eV to 20 eV split into 8000 grid points. This is chosen to be significantly higher than the default used by VASP (301 points) for better resolution of narrower peaks in the DOS plot. We use the Linear Tetrahedron method with Blochl corrections for smearing. This method linearly interpolates the energy eigenvalues ε_{ik} between subsequent k-points [45]. It performs well for semiconductors and insulators due to Blochl's corrections, which remove the quadratic error inherent in the linear tetrahedron method [55]. We use the SCAN as the XC functional for these calculations, too.

The output files for the DOS calculation from VASP are parsed using a python code using the Pymatgen module and its pymatgen.io.vasp.outputs.Vasprun, pymatgen.electronic_structure.core. Orbital, Spin, OrbitalType and

pymatgen.core.periodic_table.Element classes [52]. We plot the density of states (states/eV) as a function of energy (eV) with up-spin and down-spin states plotted as positive (above y = 0) and negative states (below y = 0), respectively. All the energies are plotted relative to the VBM energy, considering the energy of the VBM (E_{VBM}) as 0 eV. Instead of plotting the energies relative to the Fermi level, which is conventionally done, we choose the above reference as the Fermi level is calculated as the energy of the highest occupied electronic state by VASP, which includes the contributions from smearing, which need not be physically relevant. We verify the more accurate prediction of band gap using the tetrahedron method versus those from the Gaussian method for smearing by trying both on DOS calculations on renowned semiconductors. We compare the band gaps of a few stable and metastable compounds using the tetrahedron method of smearing with those obtained by using Gaussian smearing.

It is also well-known that semi-local functionals like GGA and meta-GGA functional underestimate the band-gap [7]. Experimentally, the band gap of the system is defined as the difference between the energy of the $(n+1)^{th}$ state of the system with (n+1) electrons and the energy of the n^{th} state of the system with *n* electrons. However, with the Kohn-Sham framework, we calculate the energy difference between the $(n+1)^{th}$ state and the n^{th} state, both with only *n* electrons [54]. Due to the approximations made to calculate the exchange energy, the self-interaction terms in DFT are not completely cancelled, unlike the Hartree-Fock formalism, which calculates the exact exchange energy brought in by the orthogonalization of the wavefunctions and Pauli's exclusion principle [56]. The self-interaction energies depend on the occupancies, heightening the valence bands' positions and lowering the conduction bands' positions, narrowing the band gap. A remedy would be to use functionals that incorporate a fraction of the Hartree-Fock exact exchange into the total XC energy. These are called hybrid functionals (details described in next section), which are generally used to better predict band gaps.

The calculation of DOS for the stable/metastable compounds is a quick filter to exclude the compounds with high SCAN-predicted band gaps (greater than 1.6 eV) because their true band gaps would be higher, so the compounds cannot be used. We neglect the metallic compounds for further studies, as PV candidates must be semiconductors. From the study in [7], we find that the hybrid functional band gaps are underpredicted

by SCAN by a maximum of 0.7 eV. Since we prefer compounds having (true) band gaps of greater than 1.1 eV, for the compounds considered in the thesis, we set a lower bound of 0.4 eV (= 1.1 – 0.7) for the compounds considered subsequent band structure calculations, along with an upper bound of 1.5 eV for the SCAN-calculated band gap.

2.5 Band Structure Calculation

A compound's electronic band structure diagram provides complete information about its electronic structure. It is the plot of the energy of each band versus the certain specific k-points in the Brillouin zone of the crystal, which are of high symmetry. This plot makes it easy to visualize and realize direct band gaps in the material.

We use the hybrid functional HSE06 as implemented in VASP [45, 57]. It is a range-separated hybrid functional, where short-range exchange is hybrid and long-range exchange interactions are fully given by GGA, and the slowly decaying Hartree-Fock part is replaced by the corresponding PBE functional. A general range-separated hybrid functional is given as

$$E_{XC}^{hyb} = E_C^{GGA} + E_X^{GGA,lr}(\theta) + \alpha E_X^{HF,sr}(\theta) + (1-\alpha)E_X^{GGA,sr}(\theta)$$

Equation 14

Where subscripts X or C represent exchange and correlation interactions, superscripts GGA and HF represent the contributions due to GGA and Hartree-Fock frameworks, *lr* and *sr* represent long-range and short-range interactions, α represents the mixing parameter and Θ represents the screening parameter determining the range separation. For the HSE06 functional, the screening parameter is 0.2, and the mixing parameter is 0.25.

Since we find that the Pymatgen method to generate high symmetry points and plot the hybrid band structure returns flat and non-smooth bands, we use Vaspkit [58, 59] for preprocessing and postprocessing the band structure calculations. With the Vaspkit methods, we consider the primitive cell of each structure and determine the high-symmetry k-points of the Brillouin zone obtained from the primitive cell. The high-symmetry k-points are generated according to [65]. A cyclic path joining these points is interpolated where the energy eigenvalues are computed, called the k-path. The k-

path is resolved into zero-weighted k-points between the high symmetry k points. Zero-weighted k-points are points to which no weight is given in the calculation of charge density, and the convergence of total energy at these points is not considered. We use the Gamma-centred scheme to generate the k-points and set 0.04 (1/angstrom) as the resolution values for determining the zero-weighted k-points between subsequent high-symmetry points along the k-path. We use an energy cutoff of 10^{-6} eV for the band structure calculation.

After the band structure calculations are run in VASP, we use vaspkit to read the output files to generate a data file with each band's spin-up and spin-down energies along the k-path. The highest occupied band, lowest unoccupied band, the band gap, the high symmetry points where the VBM and CBM are located, the fermi energies, VBM energy and the CBM energy for each compound considered are noted. We also plot the HSE-calculated band gap and the SCAN-calculated band gap (obtained from DOS) for all the compounds considered for band structure calculation. For each compound, we plot the band structure of the spin-up and spin-down energies, relative to E_{VBM} (as explained for DOS), using a python code, with the Matplotlib library [60]. The energies given in the vaspkit outputs are relative to the fermi level; hence, we correct them to be relative to the VBM.

All the compounds with a direct band gap of 1.1 to 1.75 eV are considered for further calculations. This upper bound of 1.75 eV is higher than the typically considered upper bound of 1.5 eV, as we reason that even compounds that show slightly higher band gaps can be doped and engineered to arrive at suitable band gaps and functionalities (p-type or n-type). For the compounds with indirect band gap, we visually inspect the band structure plot and the read the data file generated by vaspkit to identify the closest direct band-gap of the compound, which we define as the minimum direct band gap seen in the compound. The rationale for identifying the closest direct band gap is that when an indirect band gap compound absorbs light, the valence band (not necessarily VBM) electrons do get excited to the conduction band position (not necessarily the CBM) vertically above in the band structure plot, with the same value of k. Although the energy absorbed might be greater than the band gap value, these transitions are allowed and can generate photocurrent if the carriers travel to the ends of the device. We consider the minimum of these transition energies needed for a conserved wave-vector. In order to make sure that there is a significant part of the

solar spectrum which can be absorbed during these vertical transitions and generate significant photocurrent, we set an upper bound of 1.75 eV for the nearest direct band gap of the indirect band gap semiconductors also, to be considered for further calculations. The compounds predicted as non-metals with SCAN-DOS but proven here as metallic with HSE are neglected for further calculations.

2.6 Effective Mass Calculation

We consider the compounds calculated to be stable/metastable and have a suitable HSE06-calculated band gap for effective mass calculations.

The energy of a carrier can be written as a sum of its kinetic and potential energy. For a free electron, its potential energy is zero, and its kinetic energy is $\frac{\hbar^2}{2m}k^2$ where m is its (rest) mass. However, for a carrier electron in the conduction band of a semiconductor with weak periodic potential, if it is near the CBM in the band structure, its total energy (conduction band energy) is

$$E_c = E_{CBM} + \frac{\hbar^2}{2m_e^*}k^2$$

Equation 15

Where E_{CBM} represents its potential energy (here, indicative of the relative height of the CBM) and m_e^* is the effective mass of the electron for the parabolic approximation written above to hold [73]. The parabolic approximation approximates the band structure near the CBM (and VBM) to be parabolic in shape. Similarly, for a carrier hole in the valence band near the VBM, its energy (valence band energy) is

$$E_v = E_{VBM} - \frac{\hbar^2}{2m_h^*}k^2$$

Equation 16

Where E_{VBM} is the energy of the valence band maximum and m_h^* is the effective mass of the carrier hole. The effective mass of carriers is different from the rest mass, and signifies the strength of the carrier bound to the periodic potential. Given a band structure, the effective masses can be calculated for the carrier electrons near the CBM or near any local minimum in the conduction band so that derivative of energy $\frac{\partial E}{\partial k} = 0$, and the other terms in the Taylor expansion of *E* versus *k* near E_{CBM} can be neglected. At k-points which do not show a local minimum in the conduction bands,

like the case of a k-point with the nearest direct band gap, the above formula would only be an approximate description of the carrier electron effective mass at the k-point. The corresponding argument with the local maximum of the valence band for calculating the carrier hole effective mass also holds. From the above equations, the electron and hole effective masses are

$$m_e^* = \frac{\hbar^2}{\left(\frac{\partial^2 E_c}{\partial k^2}\right)}$$

$$m_h^* = \frac{-\hbar^2}{(\frac{\partial^2 E_v}{\partial k^2})}$$

Equation 17

As we see from the above expressions for effective mass, electrons tend to have positive effective masses, and holes tend to have negative effective masses. The effective masses are inversely proportional to the curvature of the band extrema at which they are calculated. Here, we calculate the effective masses of the carriers with respect to the electron rest mass, and divide the effective masses by the rest mass, to obtain m_h^{eff} and m_e^{eff}. The importance of carrier effective masses for the thesis is described as follows. The current density of the charge carrier due to the built-in potential at the p-n junction edge is proportional to the mobility of the carrier. The mobility of the carrier decreases with increasing effective mass, and the relation varies based on different approximations [61]. Therefore, carriers with low (magnitude of) effective masses tend to travel faster to the charge collection edges with a lower probability of recombination and can thus produce larger currents. The band structures showing the magnitudes of effective masses less than one are preferred.

In the thesis, we calculate the effective masses of the compounds considered, as described below. For each compound, we consider the conduction band and valence band energy values of k-path lengths of a maximum of 0.3 angstrom inverse around the k-value corresponding to the local extrema (at the VBM and CBM k-points for direct band gap candidates and the corresponding k-point where the nearest direct band gap is found for the nearest-direct band gap candidates). With the local k-points and energies taken, we perform a biquadratic interpolation of the local k-points and the valence and conduction band energies, with the local k-points split into 10,000 equally-spaced points. The valence and conduction band energies for the 10,000 points are

calculated with the biquadratic interpolation with a python script written using the Scipy module's scipy.interpolate.interp1d class [62]. This class constructs a biquadratic function to predict the interpolated energies as a function of the interpolated k-points. We choose biquadratic interpolation as linear interpolation gives discontinuous derivatives and quadratic interpolation gives discontinuous double derivatives, both of which would give spurious effective mass values.

Since the local k-points, conduction and valence band energies are equally spaced, we use the central-difference method to calculate the double derivative of the interpolated energies with respect to the interpolated local k-points. The following is the formula used.

$$\frac{\partial^2 E}{\partial k^2}(i) \approx \frac{E(i+1) - 2E(i) + E(i-1)}{(k_i - k_{i-1})^2}$$

Equation 18

E(i) is the energy of the i^{th} interpolated point, and k_i is the corresponding value of *k*. The value of *i* is chosen such that k_i is closest to the k-value of the extrema. With the values of double derivatives calculated using the above formula, we substitute these values in the equations to find the effective masses of electrons and holes.

2.7 Point defect formation energy

We calculate the point defect formation energies of all the compounds which are stable/metastable and show suitable HSE06-calculated band gaps. For photovoltaic applications, defects are considered unfavourable as they introduce trapped states for the carriers, hindering their drift and diffusion. Therefore, we perform these calculations for the candidates considered to ensure that the compounds do not thermodynamically (and readily) form defects. We consider only intrinsic point defects in the compounds as modelling extrinsic defects requires various types of external atoms to be considered at different sides, and other types of defects like line defects are typically beyond the scale of conventional DFT calculations. Point defects in compounds are irregularities that occur at a single or multiple points in a crystal. Antisite defects occur when an extra atom (of either of the types in the crystal) occupies a site of another atom type in the crystal. These are represented as B_A where an atom of type B occupies a site of atom type A. In this thesis we consider antisite-pairs of the cations present in each compound. These are represented as A_B+B_A,

where A and B are any two cation types in the compound. We do not consider antisite defects with the anion in the compound, due to the chemical intuition that the local environment of a cation would be very different from that of an anion in a crystal. Therefore, bringing about antisites that involve anions would be thermodynamically unstable, as each compound has only one anion type, and antisites with the anion would always involve a cation or its site. Vacancy defects occur when an atom from a site is missing, creating an empty site. These are represented by X_A, denoting a vacancy at an A atom site. We consider a single vacancy of all atom-types in the structure for each compound.

For constructing all the defects in each compound, we take a supercell size of the structure such that the length of each of the translational vectors in the supercell is greater than 8 angstroms. We impose this condition to avoid defect-defect interaction of one defective site with its periodic image along either of the directions.

For the formation of a defect with the removal or addition of atoms of types $i \in \{A, B, C \ldots\}$ in the compound, we assume that the compound (here, an open system) is in equilibrium with a reservoir of atoms i, with the chemical potentials (μ_i) of all i being equal in both the system and the reservoir. Thus, the compound is a system forming a Grand-Canonical ensemble with constant μ_i (for all i considered to form the defect), volume V and temperature T being constant through the defect formation process. Therefore, the grand potential (grand canonical energy, φ) of the system is the thermodynamic potential apt to describe the feasibility of defect formation in the system. For a configuration or state of the system, its grand potential is given by

$$\phi = E - \sum_i N_i \mu_i$$

Equation 19

Where N_i represents the total number of atoms of type i in the system and E is the total energy of the system, since $G \approx E$. Along the defect formation process, the defect formation energy $\Delta_{dfct}\phi$ or $\Delta_{dfct}E$ is given as

$$\Delta_{dfct}\phi = \phi_{dfct} - \phi_{pris} = \left\{E_{dfct} - \sum_i (N_i + n_i)\mu_i\right\} - \left\{E_{pris} - \sum_i (N_i)\mu_i\right\}$$
$$= E_{dfct} - E_{pris} - \sum_i n_i\mu_i$$

Equation 20

Where the subscript *pris* is the pristine state and *dfct* refers to the defected state created by adding ($n_i > 0$) or removing ($n_i < 0$) n_i atoms of the type *i* for neutral defects (with atoms being removed or added as a whole, without charge) [7, 63]. A negative defect formation energy implies that the defect formation is thermodynamically feasible. The chemical potential terms in antisite pairs cancel out since there is no net addition or removal of any atom when two atoms of the system swap their sites. For the vacancy and antisite pairs considered for each compound, we exclude the compounds that show a negative defect formation energy for either of the defects. The range of chemical potentials μ_i for each stable compound is found in the convex hull diagram of the compound. We consider the range of chemical potentials μ_i for which the compound is stable, using the same PhaseDiagram class of pymatgen [52] used for generating the convex hull. If the compound is stable, it forms a part of many Gibbs triangles (or tetrahedra), each with a unique value of μ_i such that the compound and the other phases in the Gibbs triangle are in equilibrium. If the compound is metastable, its energy is decreased by its E_{hull} value (and further by 1 meV) such that it lies on the hull with the same average composition. Upon considering all the Gibbs triangles, we consider the range of chemical potentials μ_i for which the compound is stable. Accordingly, these chemical potential values confer a range of defect formation energies.

We find all the symmetrically unique sites occupied by each atom type by using the pymatgen.transformations.advanced_transformations.EnumerateStructureTransformation class of Pymatgen [52], where we generate structures with different single-vacant configurations of each atom type. The duplicates in the structures are removed using an Ewald summation [64] criterion with a precision of 10^{-5} eV. With the unique sites for each atom identified, we initialize supercell structures with single vacancies of each atom type at each unique site. For the cation antisite pairs, we swap the positions of each site of the first cation with each of the second cation in the supercells.

Each defective structure is structurally relaxed with the same XC functional used, energy and force cutoffs for bulk structure relaxation (as described in Section 2.2). However, during relaxation, we sample only the Gamma point in the Brillouin zone and do not let the translational vectors (a, b, c) change. The minimum total DFT energy among for these relaxed configurations of the same defect type is taken as its E_{dfct}. We perform a single SCF calculation of the pristine converged structure with the same supercell size as that used for defect initialization, sampling only the Gamma point in the Brillouin zone, and consider its total DFT energy as E_{pris}. We consider the compounds whose values of $\Delta_{dfct}E$ for most defects is greater than 1 eV, as such defects have caused minimal efficiency losses in previous studies [7].

The candidates that satisfy all the criteria described in this chapter are considered prospective beyond-Si PV materials.

Chapter 3 **Results and Discussion**

This chapter describes the results obtained and their interpretation

3.1 Structural relaxation and Polymorph stability

K_4ZnP_2 is one of the structural templates for all the compounds of the A_4BX_2 class of compositions. Its structure belongs to the R-3mH space group. It consists of alternating tetrahedral potassium (edge-shared with other tetrahedra and trigonal potassium) and linearly coordinated zinc, with phosphorus present at the vertices of the tetrahedra, triangles and are the atoms to which the zinc atoms are coordinated. Li_4SrN_2, the other structural template of the A_4BX_2 class has its conventional structure in the $I4_1/amd$ space group having trigonal and linear lithium atoms with strontium tetrahedra sharing two edges with triangles created by nitrogen atoms flanking lithium atoms.

$LiCaGaN_2$ of the $P2_1/c$ space group is one of the structural templates for $ABCX_2$ class, having layers of gallium and lithium-centred tetrahedra sharing edges with the calcium octahedra that they are in between. $LiSrGaN_2$, the other template, has the structure in C2/m space group, which is not layered, but also consists of strontium octahedra sharing edges with lithium and gallium tetrahedra. The structural templates for the BB'B"X_2 compounds are described in [7] (refer to Table 2 for structures). Tables 5, 6 and 7 show the list of compositions of each class and the energies of structures relaxed from the two templates for each composition.

Table 5: Energies in (eV/formula unit) of structures initialized from both template space groups for each composition (first column) of the A_4BX_2 class. Space groups shown in bold indicate that the composition they are adjacent to serves as template structures for the space group. The space groups shaded with green represent the space group of the ground state (more stable) polymorph with relatively lesser energy. For the energies shown as NOT CONVERGED, the DFT calculation does not converge after many iterative runs; therefore, we consider the other polymorph for further calculations.

A4BX2	Template Space group	Energy (eV/f.u.)	A4BX2	Template Space group	Energy (eV/f.u.)
	R-3mH	-71.21676667		R-3mH	-62.34583333
K4ZnP2	I41/amd	-70.38115	**K4MgP2**	I41/amd	-60.9628
	R-3mH	-65.0909		R-3mH	-55.93863333
K4ZnN2	I41/amd	-63.8976	**K4MgN2**	I41/amd	NOT CONVERGED
Na4ZnP2	R-3mH	-54.62356667	**Na4MgP2**	R-3mH	-45.9282

	I41/amd	-53.47615		I41/amd	-46.2799
	R-3mH	-49.5703		R-3mH	-40.59463333
Na4ZnN2	I41/amd	-48.7302	**Na4MgN2**	I41/amd	-40.4398
	R-3mH	-66.67396667		R-3mH	-79.09726667
K4CaP2	I41/amd	-67.39725	**K4SrP2**	I41/amd	-79.9742
	R-3mH	-59.87433333		R-3mH	-72.30353333
K4CaN2	I41/amd	NOT CONVERGED	**K4SrN2**	I41/amd	NOT CONVERGED
	R-3mH	-50.5059		R-3mH	-64.2081
Na4CaP2	I41/amd	-50.97225	**Na4SrP2**	I41/amd	-63.78815
	R-3mH	-44.66533333		R-3mH	-56.96633333
Na4CaN2	I41/amd	-45.1541	**Na4SrN2**	I41/amd	-57.7215
	R-3mH	-48.25666667		R-3mH	-39.78316667
Li4ZnP2	I41/amd	-47.96545	**Li4MgP2**	I41/amd	-40.6728
	R-3mH	-45.04496667		R-3mH	-36.33676667
Li4ZnN2	I41/amd	-43.93915	**Li4MgN2**	I41/amd	-36.78495
	R-3mH	-44.44413333		R-3mH	-59.1812
Li4CaP2	I41/amd	-45.52905	**Li4SrP2**	I41/amd	-58.18565
	R-3mH	-41.79583333		R-3mH	-53.91733333
Li4CaN2	I41/amd	-41.961	**Li4SrN2**	**I41/amd**	-54.22845

Table 6: Energies in (eV/formula unit) of structures initialized from both template space groups for each composition (first column) of the $ABCX_2$ (shown as CBAX2) class.

CBAX2	Template Space Group	Energy (eV/f.u.)	CBAX2	Template Space Group	Energy (eV/f.u.)
	P21/c	-51.020975		P21/c	-47.31145
AlCaKP2	C2/m	-50.37726667	**AlZnLiP2**	C2/m	-46.75793333
	P21/c	-48.859975		P21/c	-46.046375
AlCaKN2	C2/m	-50.38825	**AlZnLiN2**	C2/m	-46.14393333
	P21/c	-58.913175		P21/c	-55.209825
GaCaKP2	C2/m	-58.35271667	**GaZnLiP2**	C2/m	-54.68053333
	P21/c	-55.6156		P21/c	-52.672625
GaCaKN2	C2/m	-54.64068333	**GaZnLiN2**	C2/m	-52.53588333
	P21/c	-75.8469		P21/c	-71.8963
InCaKP2	C2/m	-75.45893333	**InZnLiP2**	C2/m	-71.48363333
	P21/c	-71.76775		P21/c	-68.182175
InCaKN2	C2/m	-71.14031667	**InZnLiN2**	C2/m	-68.35626667

	P21/c	-45.1784		P21/c	-48.8905
AlMgKP2	C2/m	-44.89666691	**AlZnNaP2**	C2/m	-48.3521
	P21/c	-44.42155		P21/c	-47.674625
AlMgKN2	C2/m	-42.84921667	**AlZnNaN2**	C2/m	-46.94056667
	P21/c	-53.170575		P21/c	-56.83675
GaMgKP2	C2/m	-52.81855	**GaZnNaP2**	C2/m	-56.20253333
	P21/c	-51.050025		P21/c	-53.409675
GaMgKN2	C2/m	-49.74195	**GaZnNaN2**	C2/m	-53.37235
	P21/c	-70.089525		P21/c	-73.556275
InMgKP2	C2/m	NOT CONVERGED	**InZnNaP2**	C2/m	-73.16261667
	P21/c	-66.986425		P21/c	-69.319125
InMgKN2	C2/m	-66.12773333	**InZnNaN2**	C2/m	-69.3898
	P21/c	-47.1296		P21/c	-53.443775
AlCaNaP2	C2/m	-46.8397	**AlZnKP2**	C2/m	-52.46573333
	P21/c	-45.12695		P21/c	-51.34515
AlCaNaN2	C2/m	-44.88161667	**AlZnKN2**	C2/m	-50.38825
	P21/c	-54.969375		P21/c	-61.313625
GaCaNaP2	C2/m	-54.7188	**GaZnKP2**	C2/m	-60.46196667
	P21/c	-51.87555		P21/c	-57.653725
GaCaNaN2	C2/m	-51.6562	**GaZnKN2**	C2/m	-57.02358333
	P21/c	-71.912425		P21/c	-77.18055
InCaNaP2	C2/m	-71.56551667	**InZnKP2**	C2/m	-77.33985
	P21/c	-67.91585		P21/c	NOT CONVERGED
InCaNaN2	C2/m	-67.62625	**InZnKN2**	C2/m	-73.40141667
	P21/c	-41.220975		P21/c	-58.631075
AlMgNaP2	C2/m	-40.91716466	**AlSrLiP2**	C2/m	-58.44940043
	P21/c	-40.58675		P21/c	-56.629875
AlMgNaN2	C2/m	-39.71827523	**AlSrLiN2**	C2/m	-56.78393333
	P21/c	-49.132275		P21/c	-66.45828518
GaMgNaP2	C2/m	-48.76801667	**GaSrLiP2**	C2/m	-66.30711667
	P21/c	-46.678225		P21/c	-63.351125
GaMgNaN2	C2/m	-46.37096667	**GaSrLiN2**	**C2/m**	-63.40331667
	P21/c	-65.900975		P21/c	-83.322575
InMgNaP2	C2/m	-65.59811667	**InSrLiP2**	C2/m	-83.02698333
InMgNaN2	P21/c	-62.42865	**InSrLiN2**	P21/c	-79.3352

	C2/m	-62.26741667		C2/m	-79.16768333
	P21/c	-46.036975		P21/c	-59.826975
AlCaLiP2	C2/m	-45.6986	**AlSrNaP2**	C2/m	-59.59675
	P21/c	-44.68215		P21/c	-57.2258
AlCaLiN2	C2/m	-44.59045298	**AlSrNaN2**	C2/m	-57.13246667
	P21/c	-53.838		P21/c	-67.686975
GaCaLiP2	C2/m	-53.53628333	**GaSrNaP2**	C2/m	-67.48625
	P21/c	-51.32235		P21/c	-64.070625
GaCaLiN2	C2/m	-51.14785	**GaSrNaN2**	C2/m	-63.9546
	P21/c	-70.589125		P21/c	-84.726525
InCaLiP2	C2/m	-70.16438333	**InSrNaP2**	C2/m	-84.4079
	P21/c	-67.02065		P21/c	-80.299725
InCaLiN2	C2/m	-66.78461667	**InSrNaN2**	C2/m	-80.07685
	P21/c	-39.76395		P21/c	-63.530125
AlMgLiP2	C2/m	-39.44181951	**AlSrKP2**	C2/m	-63.01068333
	P21/c	-39.4846		P21/c	-60.86045
AlMgLiN2	C2/m	-39.1678	**AlSrKN2**	C2/m	-59.86578333
	P21/c	-47.544675		P21/c	-71.490625
GaMgLiP2	C2/m	-47.20435	**GaSrKP2**	C2/m	-70.98761667
	P21/c	-45.868925		P21/c	-67.669275
GaMgLiN2	C2/m	-45.5816	**GaSrKN2**	C2/m	-66.89346667
	P21/c	-64.165825		P21/c	-88.386325
InMgLiP2	C2/m	-63.99758333	**InSrKP2**	C2/m	-88.14915
	P21/c	-61.341625		P21/c	-83.883925
InMgLiN2	C2/m	-61.42073333	**InSrKN2**	C2/m	-83.44911667

Table 7: Energies in (eV/formula unit) of structures initialized from both template space groups for each composition (first column) of the BB'B"X_2 class.

BB'B"X2	Template Space Group	Energy (eV/f.u.)	BB'B"X2	Template Space Group	Energy (eV/f.u.)
	P-3m1	-13.39882		P-3m1	-10.15126
CaSrZnN2	**I4/mmm**	-13.57988	**MgCaZnN2**	I4/mmm	-9.61476
	P-3m1	-14.23022		P-3m1	-10.7445
CaSrZnP2	I4/mmm	-14.21175	**MgCaZnP2**	I4/mmm	-10.13907
MgSrZnN2	P-3m1	-12.57084	**MgCaSrN2**	P-3m1	-11.902

	I4/mmm	-11.92891		I4/mmm	-11.81554
	P-3m1	-13.27352		P-3m1	-12.62978
MgSrZnP2	I4/mmm	-13.00961	**MgCaSrP2**	I4/mmm	-12.51662

In the A_4BX_2 class, we find that eleven compositions are stable in the $I4_1/amd$ structure and thirteen compositions favour the R-3mH structure, indicating equal preference of structures of both the space groups for this composition class. We find that many of the Li-containing compounds of this class prefer the $I4_1/amd$ structure, since the structures are initialized from Li_4SrN_2. This could be due to the larger cations (Na and K) preferring tetrahedral and trigonal sites (as in the R-3mH) structure and lithium ions preferring linear and trigonal coordination. For the structural templates K_4ZnP_2 and Li_4SrN_2, we find that their corresponding experimentally observed structures are relatively stable with our DFT calculations over the other structure initialized for them. Among the 72 compositions of the $ABCX_2$ class, only nine compositions favour the C2/m space group. The rest have the $P2_1/c$ space group structures as being relatively stable. Six out of nine compositions that favour the C2/m space group contain zinc, and we find that the initialization in the C2/m structure allows for the local environments of the zinc to change from octahedral to tetrahedral (favoured due to its relatively small ionic radius) upon relaxation. Here, the template structures $LiSrGaN_2$ and $LiCaGaN_2$ are also stable in their respective experimentally observed space groups. Our studies match those in [7], where $CaSrZnN_2$ is more stable in the I4/mmm polymorph and $CaSrZnP_2$ is more stable in the P-3m1 polymorph. The other BB'B"X_2 compositions considered here which contain magnesium, prefer the P-3m1 structures.

3.2 Convex hull calculations

Table 8 describes the chemical space, the compounds considered in each space and their calculated DFT-energies used to construct the convex hull of stability of each of the compounds (composition + stable structure, as determined in 3.1) of each composition class. The subsidiary compounds of the Sr-N, Sr-P, Ca-N, Ca-P, Zn-N and Zn-P space are taken from [7]. The subsidiary compounds of other spaces are considered from ICSD [47].

Table 8: The binary (leftmost column), ternary (fourth column) and unary (elements, bottom leftmost column) chemical spaces considered, the subsidiary compounds found in ICSD for each space, and the calculated DFT

energies (eV/formula unit) obtained in this study. The hyphen (-) under compounds indicates that no compound of the chemical space is present in ICSD.

Binary space	Compounds	Energy (eV/f.u.)	Ternary space	Compounds	Energy (eV/f.u.)
	Sr2N	-55.97113333		CaSr2N2	-76.3909625
	Sr3N2	-88.8952625	**Ca-Sr-N**	SrCa2N2	-64.3945
	SrN	-32.9699625		ZnCa2N2	-55.7717
Sr-N	SrN2	-42.8138	**Ca-Zn-N**	CaZn2N2	-57.963
	Sr3P2	-93.8256625		ZnSr2N2	-80.36695
	SrP	-35.12561667	**Sr-Zn-N**	SrZn2N2	-70.0497
	Sr3P4	-116.2264375		SrCa2P2	-68.9515
	SrP2	-45.86703333	**Ca-Sr-P**	CaSr2P2	-81.0640875
	SrP3	-56.525425		CaZn2P2	-61.4262
Sr-P	Sr3P14	-221.749	**Ca-Zn-P**	ZnCa2P2	-58.4502
	Ca2N	-31.2772		SrZn2P2	-74.0288
	Ca3N2	-52.2924	**Sr-Zn-P**	ZnSr2P2	-83.475
Ca-N	CaN2	-30.18805	**Ca-Mg-N**	CaMg2N2	-43.2841
	CaP3	-43.7726	**Sr-Mg-N**	SrMg2N2	-55.4011
	Ca5P8	-145.0698	**Zn-Mg-N**	-	
	CaP	-22.53321667	**Ca-Mg-P**	-	
Ca-P	Ca3P2	-55.92163333	**Sr-Mg-P**	-	
Zn-N	Zn3N2	-59.144375	**Zn-Mg-P**	Mg1.75Zn1.25P2	-47.3332
	ZnP4	-55.71505		LiCaN	-23.699475
	ZnP2	-35.2028875	**Li-Ca-N**	Li2Ca3(N2)3	-95.95625
Zn-P	Zn3P2	-62.3744	**Li-Ca-P**	-	
	MgP4	-48.5582	**Na-Ca-N**	-	
Mg-P	Mg3P2	-39.8105625	**Na-Ca-P**	Na22Ca13P16	not converged
Mg-N	Mg3N2	-38.383	**K-Ca-N**	-	
	Li3N	-18.2739	**K-Ca-P**	-	
	LiN3	-31.0428	**Li-Sr-N**	LiSrN	-35.85415
	LiN2	-21.91485	**Li-Sr-P**	LiSrP	-28.1832
Li-N	LiN5	-48.4472	**Na-Sr-N**	-	
	Li3P	-20.6394		Na2Sr3P4	-125.74665
	LiP	-13.958375	**Na-Sr-P**	NaSrP	-39.81176667
	LiP5	-55.852225	**K-Sr-N**	-	
	LiP7	-76.738475	**K-Sr-P**	-	
Li-P	Li3P7	-84.07745	**Li-Zn-N**	LiZnN	-26.3482

	Na3N	-21.2792	**Li-Zn-P**	LiZnP	-27.5617
	Na3N8	not converged	**Na-Zn-N**	-	
	NaN2	-23.3501	**Na-Zn-P**	NaZnP	-29.61495
Na-N	NaN3	-32.7537	**K-Zn-N**	K2Zn(N3)4	-141.090825
	NaP	-15.60635	**K-Zn-P**	KZnP	-33.9183
	Na3P	-24.88475		KZn4P3	-48.2064
	Na3P11	-131.254875	**Li-Mg-N**	LiMgN	-19.08775
Na-P	NaP7	-78.5973375		LiMgN	-19.0956
	KN3	-37.12105	**Li-Mg-P**	LiMgP	-19.2527
K-N	K3N	-32.54195		LiMgP	-20.4185
	KP	-19.8148125	**Na-Mg-N**	-	
	K3P	-36.7677	**Na-Mg-P**	-	
	K4P3	-68.0743	**K-Mg-N**	-	
K-P	K4P6	-101.2078	**K-Mg-P**	KMgP	-26.1259
Al-P	AlP	-19.6364		Ca3Al2N4	-94.041025
Al-N	AlN	-20.44915	**Ca-Al-N**	Ca3AlN3	-73.265425
Ga-P	GaP	-27.6615	**Ca-Al-P**	Ca3Al2P4	-96.58585
Ga-N	GaN	-26.8973		CaGaN	-37.8902
	InP3	-64.9659	**Ca-Ga-N**	Ca5Ga2N4	-128.38165
In-P	InP	-44.3705		CaGa2P2	-66.91535
In-N	InN	-42.7904	**Ca-Ga-P**	Ca3Ga2P4	-112.22105
ELEMENTS				Ca4In2N	-120.2521
Unary space	**Elements**	**Energy (eV/f.u.)**	**Ca-In-N**	Ca2InN	-65.3638
	Li	-2.34055	**Ca-In-P**	Ca3InP3	-101.3111
	Na	-4.2087	**Sr-Al-N**	Sr3Al2N4	-130.8655
	K	-8.338	**Sr-Al-P**	Sr3Al2P4	-134.5162
	Ca	-9.645		Sr3Ga3N5	-170.84285
	Sr	-22.292375	**Sr-Ga-N**	Sr3Ga2N4	-143.927875
	Mg	-4.98395	**Sr-Ga-P**	Ga2Sr3P4	-150.2137
	Zn	-13.4946	**Sr-In-N**	Sr4In2N	-169.7946
	Al	-7.749525		Sr3InP3	-139.2393
	Ga	-16.344025		Sr3In2P4	-183.93495
	In	-33.3106	**Sr-In-P**	SrIn2P2	-113.467
	N	-9.2835		Mg3Al2N4	-77.7765
	P	-10.222525	**Mg-Al-N**	Mg3AlN3	-57.68613333

	Mg-Ga-N	GaMg3N3	-64.9422
	Li-Al-N	Li3AlN2	-39.65955
	Li-Al-P	Li3AlP2	-40.772425
	Li-Ga-N	Li3GaN2	-46.096325
		Li3GaP2	-48.5465
	Li-Ga-P	Li9GaP4	-89.3005
	Li-In-N	-	
	Li-In-P	Li9InP4	
	Na-Al-N	-	
	Na-Al-P	Na3AlP2	-45.0867
	Na-Ga-N	-	
		Na3GaP2	-52.85855
	Na-Ga-P	Na6GaP3	
	Na-In-N	-	
	Na-In-P	Na3InP2	-69.8687625
	K-Ga-P	K2GaP2	-56.6635625
		K3InP2	-82.1887
	K-In-P	K6InP3	-119.2852
	K-Al-N	-	
	K-Al-P	-	
	K-Ga-N	-	
	K-In-N	-	

The energies of the subsidiary compounds and the candidate compounds are used to construct the convex hulls for the corresponding chemical spaces. Here, we show the calculated convex hulls of the chemical spaces of two ternary stable compounds (Na_4ZnP_2 and K_4ZnP_2), a ternary metastable compound (Na_4MgP_2), a quaternary stable compound ($NaCaInN_2$) and a quaternary metastable compound ($NaSrInN_2$) in the following Figure 2. Figure 1 in Section 2.3 shows an unstable ternary compound (K_4SrP_2) in the phase diagram.

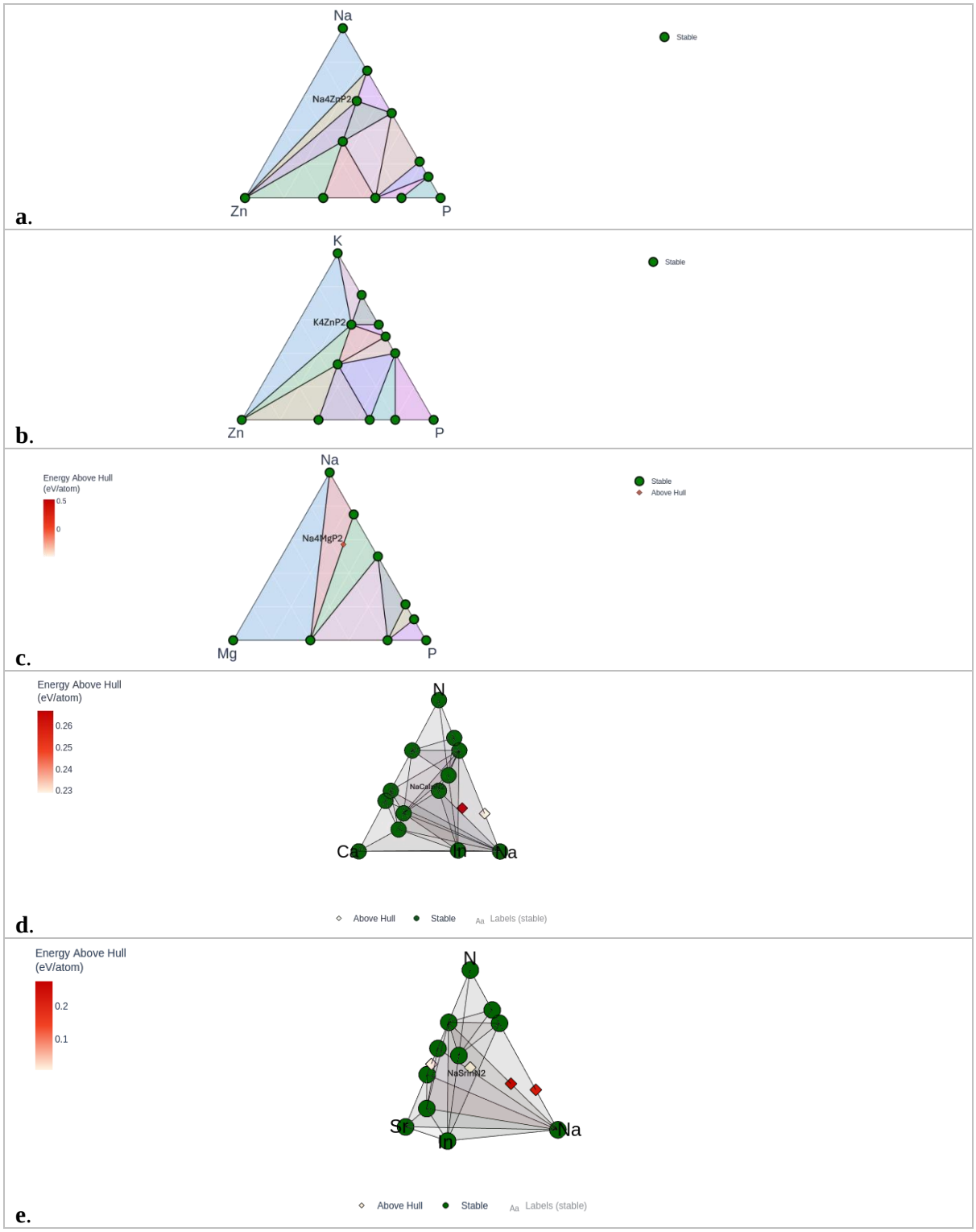

Figure 2: The phase diagrams of (a) Na_4ZnP_2, (b) K_4ZnP_2, (c) Na_4MgP_2, (d) $NaCaInN_2$ and (e) $NaSrInN_2$. Green points show stable compounds and red points show metastable or unstable points, according to the legends in the left of each plot.

Figure 3 contains the heatmap plots showing the energies above the convex hull (E_{hull}) for all compounds of each class, along with the asterisk * indicating the stable polymorph for each composition. We consider the compounds (41 out of 104

compositions) shown in blue shades (E_{hull} less than or equal to 30 meV/atom) for the next set of calculations.

Figure 3: Heatmap showing E_{hull} of all compounds of (a) BB'B"X_2 class (nan denotes repeated or invalid compositions), (b) A_4BX_2 class, $ABCX_2$ class with (c) B = Ca, (d) B = Sr, (e) B = Mg and (f) B = Zn. The asterisk (*) represents the compounds which have I4/mmm structure in (a), $I4_1$/amd structure in (b) and C2/m structure in (c), (d), (e) and (f).

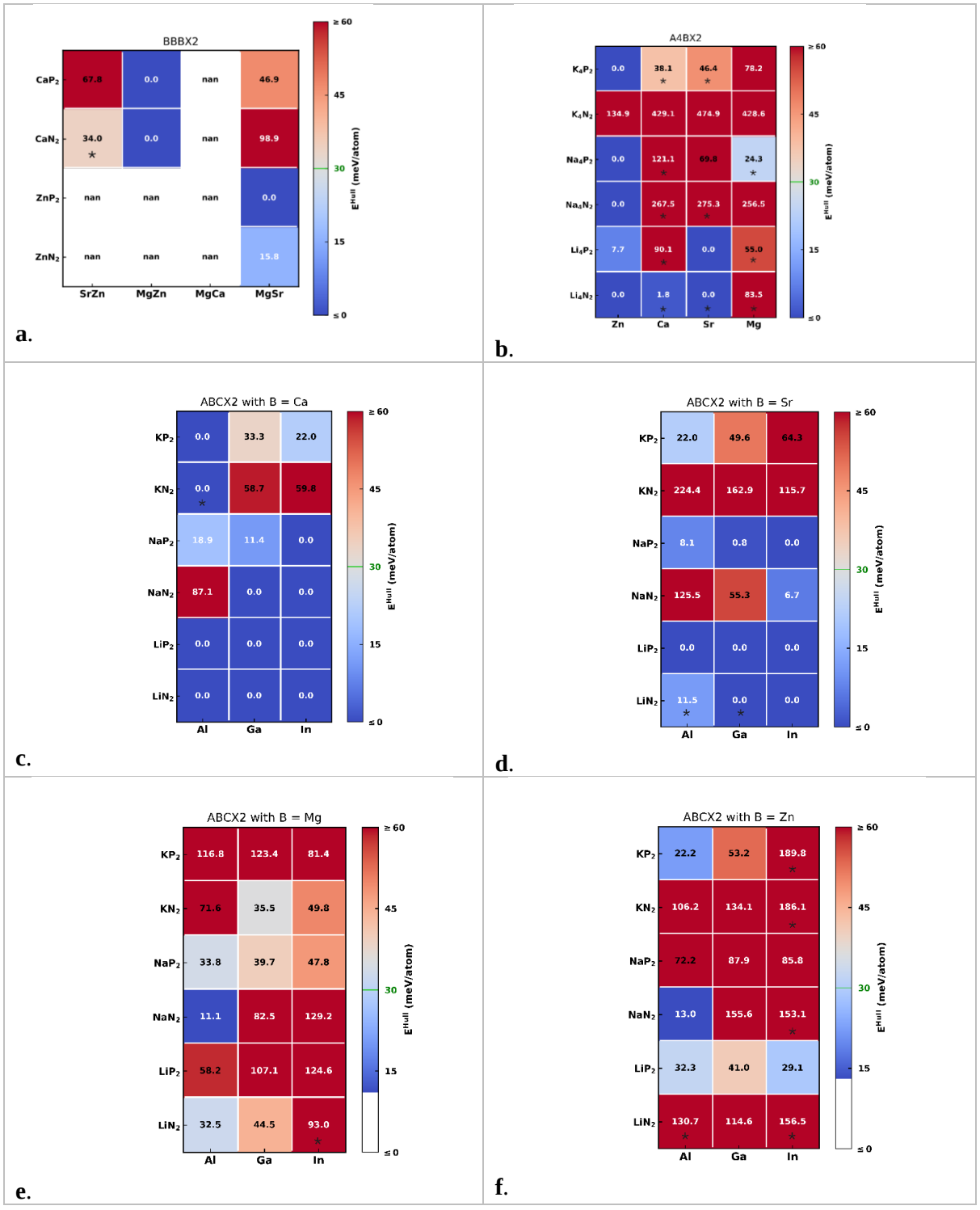

Our reported values of E_{hull} of $CaSrZnP_2$ and $CaSrZnN_2$ match those reported in [7]. In the A_4BX_2 class, potassium nitrides lie relatively high above the hull. We also find that many of the zinc-containing compounds of this class are stable, probably due to the initialization of their ground state structure from K_4ZnP_2. In the $ABCX_2$ class, all of the magnesium and zinc compounds lie above the hull, with many being significantly unstable. This could be attributed to two reasons; the first one being zinc and magnesium are ions of a relatively small ionic radius compared to strontium and calcium, which are the B elements present in both the template structures for this class, $LiSrGaN_2$ and $LiCaGaN_2$. Therefore, the replacement of magnesium or zinc in these structures has led to the structures being unstable. Despite the argument proposed that zinc-compounds populate the C2/m-stable structures due to their flexibility in this structure to change their environment from octahedral to tetrahedral, this flexibility conferred by the structure does not seem enough to stabilize the compound as a whole, to lie on the convex hull. The second reason is that all of these structures are derived from templates; hence, there could be a possibility that a previously unexplored (or unnoticed in this study) structure could be the closest template to the true thermodynamic ground states of these compounds.

3.3 Density of states

We consider 41 compounds which are stable or metastable for the calculations of electronic density of states (DOS), of which four compositions are from the $BB'B''X_2$ class, nine from A_4BX_2 class and the rest from $ABCX_2$ class. Using the DOS-interpolated band gap of certain known compounds, we verify the validity of using the linear tetrahedral smearing and compare the results with those obtained from gaussian smearing of a tight smearing width (0.01 eV), as shown in Table 9. The VBM is calculated as the highest energy among all occupied states at all k-points, and the CBM is calculated as the lowest energy among all unoccupied states at all k-points. The band gap is determined as the difference of the CBM and VBM energies. Different smearing methods cause different artificial partial occupancies close to the band edges, affecting the identification of the true VBM and CBM, hence changing the computed band gap. We see that despite the tight smearing width, gaussian smearing underpredicts the SCAN-calculated band gaps more than tetrahedral smearing.

Table 9: Interpolated band gaps (E_g) of established compounds using Tetrahedral smearing and Gaussian smearing. CZTS refers to Cu_2ZnSnS_4, with its polymorphs indicated next to it.

Compound	E_g (eV) Tetrahedral smearing	E_g (eV) Gaussian smearing
CZTS, Kesterite	0.417	0.361
CZTS, Stannite	0.276	0.22
GaAs	0.666	0.581

Tables 10 and 11, respectively show the DOS-interpolated band gaps of the $BB'B''X_2$ and A_4BX_2 compounds considered, with tetrahedral smearing and Gaussian smearing (width 0.05 eV) for comparison. We see that Gaussian smearing underpredicts the band gaps for these compounds, as shown in Table 9. Table 12 shows the DOS-interpolated band gaps for the compounds of $ABCX_2$ class, with tetrahedral smearing.

Table 10: DOS-interpolated band gaps (E_g) of $BB'B''X_2$ compounds using Tetrahedral smearing and Gaussian smearing.

$BB'B''X_2$	E_g (eV) Tetrahedral smearing	E_g (eV) Gaussian smearing
$MgSrZnP_2$	1.475	1.251
$MgSrZnN_2$	1.395	1.186
$MgCaZnP_2$	1.500	1.296
$MgCaZnN_2$	1.635	1.441

Table 11: DOS-interpolated band gaps (E_g) of A_4BX_2 compounds using Tetrahedral smearing and Gaussian smearing. _ indicates that the values are not calculated

A_4BX_2	E_g (eV) Tetrahedral smearing	E_g (eV) Gaussian smearing
K_4ZnP_2	1.312	1.048
Na_4ZnP_2	1.376	1.127
Na_4ZnN_2	0.765	0.512
Na_4MgP_2	1.230	0.982
Li_4ZnP_2	1.095	_
Li_4SrP_2	1.385	_
Li_4ZnN_2	1.470	_
Li_4CaN_2	1.696	_
Li_4SrN_2	1.290	_

Table 12: DOS-interpolated band gaps (E_g) of $ABCX_2$ compounds using Tetrahedral smearing.

$ABCX_2$	E_g (eV)
$NaMgAlN_2$	2.556
$KCaAlP_2$	2.185
$KCaInP_2$	1.702
$KCaAlN_2$	1.016
$NaCaAlP_2$	1.890
$NaCaGaP_2$	1.370
$NaCaInP_2$	1.545
$NaCaGaN_2$	1.976
$NaCaInN_2$	0.961
$LiCaAlP_2$	1.710
$LiCaGaP_2$	1.315
$LiCaInP_2$	1.440
$LiCaAlN_2$	3.255

$LiCaGaN_2$	2.711
$LiCaInN_2$	1.406
$KSrAlP_2$	2.036
$NaSrAlP_2$	1.961
$NaSrGaP_2$	1.550
$NaSrInP_2$	1.597
$NaSrInN_2$	0.946
$LiSrAlP_2$	1.686
$LiSrGaP_2$	1.356
$LiSrInP_2$	1.490
$LiSrAlN_2$	2.865
$LiSrGaN_2$	2.436
$LiSrInN_2$	1.256
$KZnAlP_2$	1.535
$NaZnAlN_2$	2.091
$LiZnInP_2$	1.066

From Table 12, with the limited data, we observe that in $ABCX_2$ compounds, for a given A and B if X = N, we find that the band gap decreases from C = Al to In. If X = P, C = Ga has the minimum band gap among C = Al, Ga, In for the same A and B. However, the data available here may not be significant enough to confirm this hypothesis. As explained in Chapter 2, we consider only the compounds with DOS-interpolated band gaps in the range of 0.4 eV to 1.5 eV for band structure calculations. Figure 4 shows the DOS plots of the compounds whose band gaps fall in the above range.

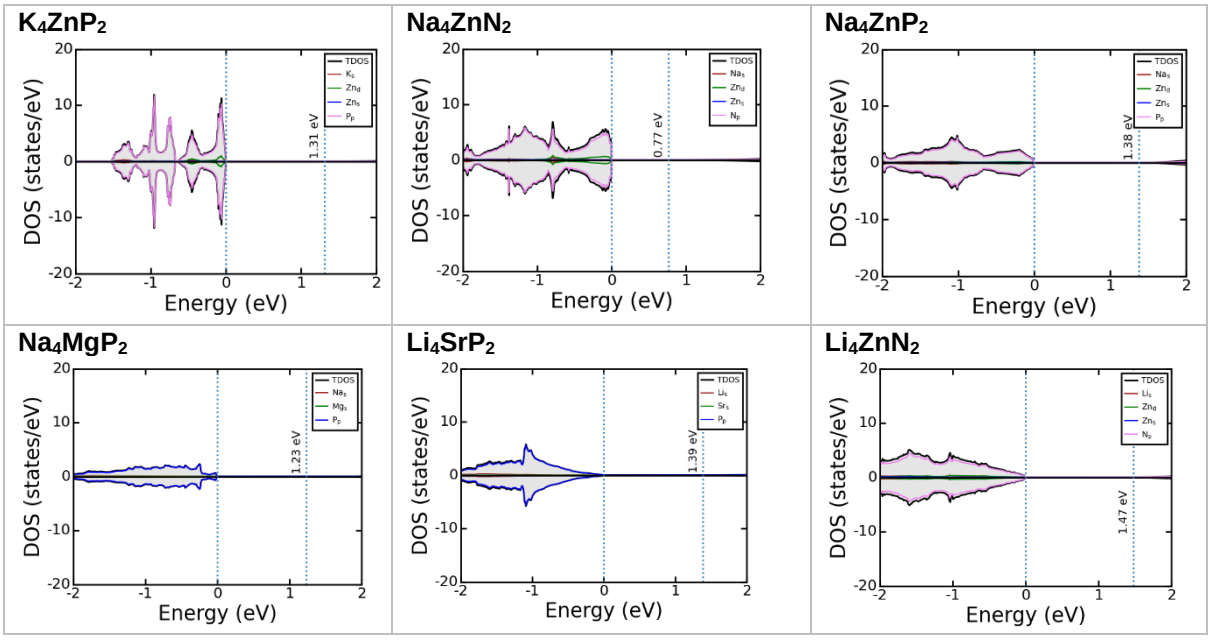

Li_4SrN_2

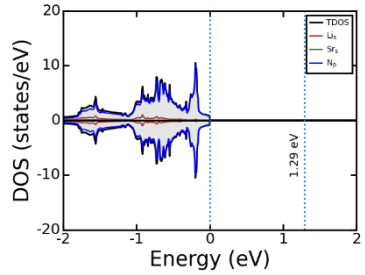

Li_4ZnP_2

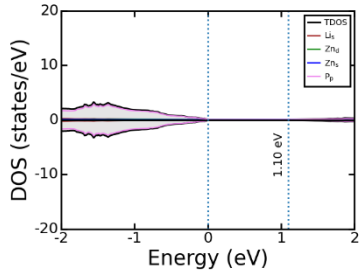

$NaSrInN_2$

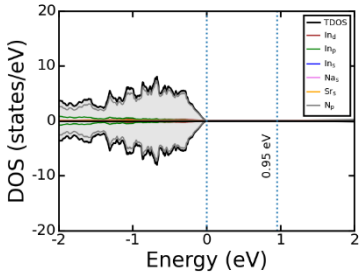

$LiZnInP_2$

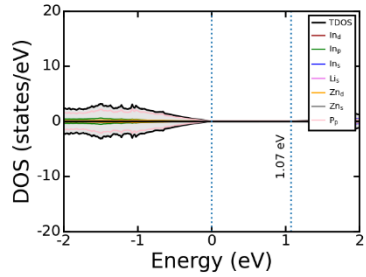

$LiCaInP_2$

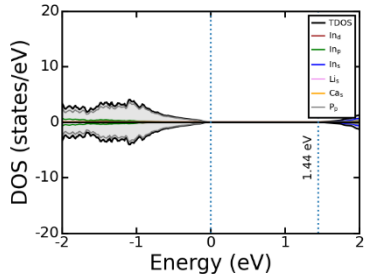

$LiCaGaP_2$

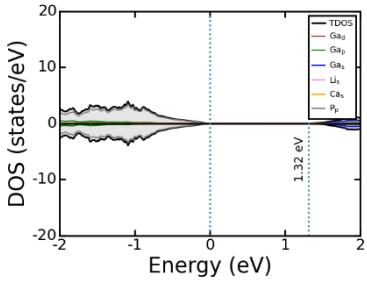

$NaCaGaP_2$

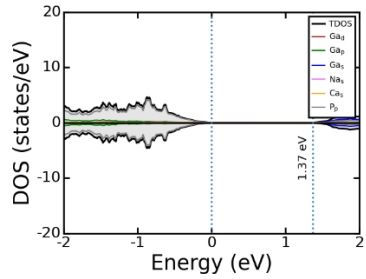

$NaCaInN_2$

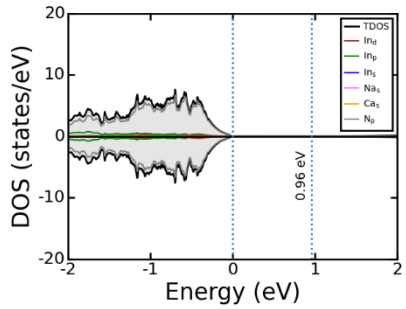

$LiCaInN_2$

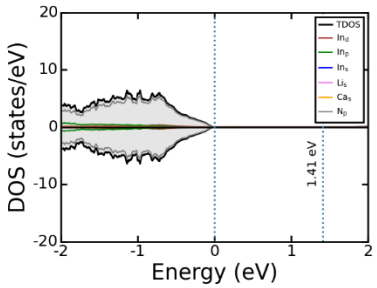

$LiSrGaP_2$

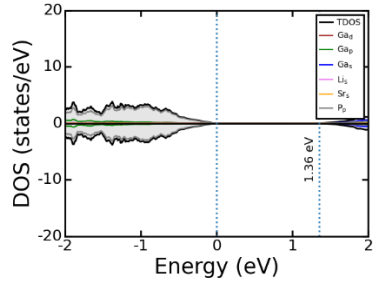

$LiSrInP_2$

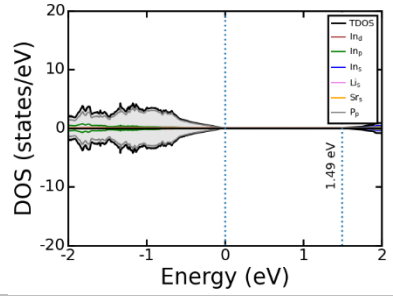

$LiSrInN_2$

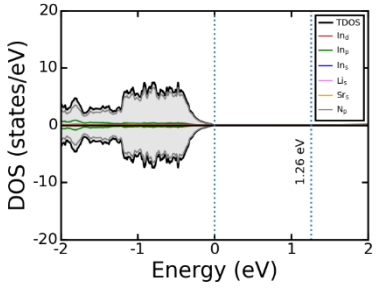

$MgSrZnP_2$

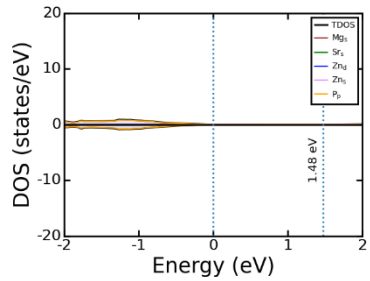

$MgSrZnN_2$

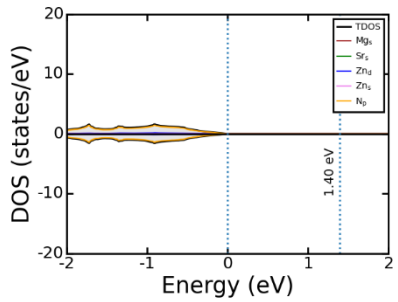

$MgCaZnP_2$

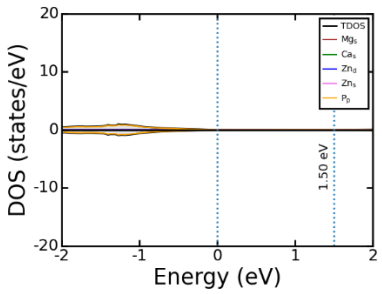

Figure 4: DOS (y-axis) v/s Energy (X-axis) plots of compounds with SCAN-calculated DOS-interpolated band gaps of 0.4 to 1.5 eV. Each cell shows the compound considered and its DOS plot with the band gap (E_g) written. The dotted blue lines represent conduction and valence band edges. The projection of the total DOS (TDOS) on each element's valence orbitals are taken, as labelled and colour-coded in the top right corner for each plot.

We observe that the BB'B"X_2 compounds have some states (per eV) near the VBM, showing weak valence electronic interactions to form the structure. In all the compounds, the p-orbitals of phosphorus (in phosphides) or nitrogen (in nitrides) contribute the most towards the electronic states near the VBM and CBM. The states corresponding to the cations overlap with these states but lie relatively lower in energy. This could possibly be due to the N_p and P_p showing few non-bonding orbitals in the compounds, which contribute to the states near the VBM. The states near the CBM could be formed due to the antibonding interactions of the N_p and P_p orbitals with the cation orbitals. In the $ABCX_2$ (mainly) and A_4BX_2 compounds, we see that the s-orbitals of A atoms do not show any states near the VBM and CBM. In the $ABCX_2$ compounds, they do not show any states in the plotted energy range. These compounds do not show s-states of the B atoms. This means that the compounds are largely stabilized by the electronic interactions of the orbitals of C atoms with those of X atoms.

3.4 Band structures and Effective mass

Figure 5 shows the HSE06-calculated band structures of the twenty-two compounds whose SCAN-calculated band gaps lie in the range of 0.4 eV to 1.5 eV.

K_4ZnP_2

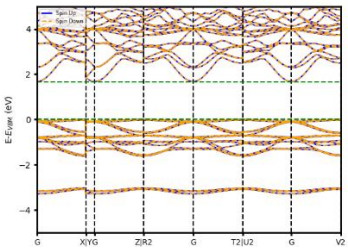

Na_4ZnN_2

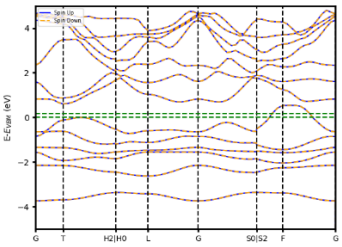

Na_4ZnP_2

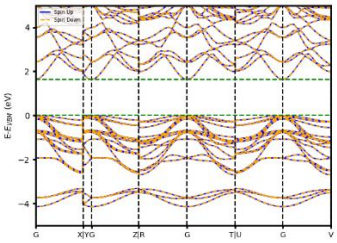

Na_4MgP_2

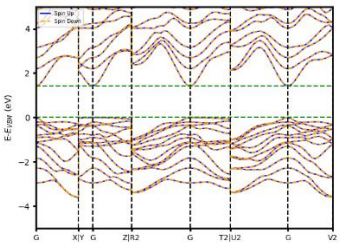

Li_4SrP_2

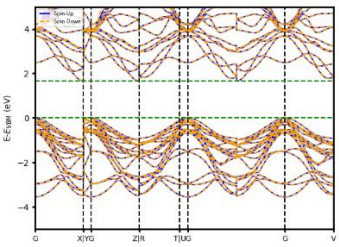

Li_4ZnN_2

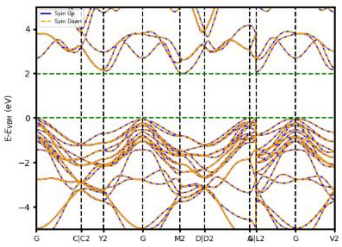

Li_4SrN_2

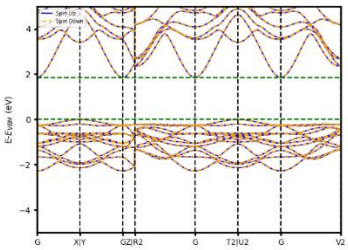

Li_4ZnP_2

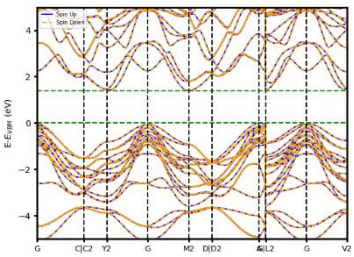

$NaSrInN_2$

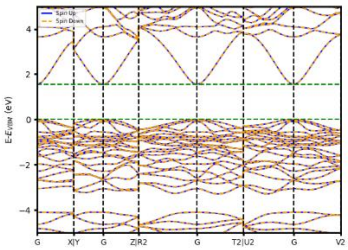

$LiZnInP_2$

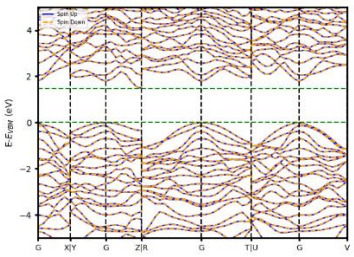

$LiCaInP_2$

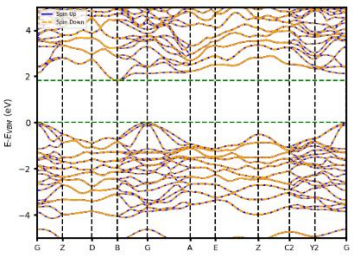

$LiCaGaP_2$

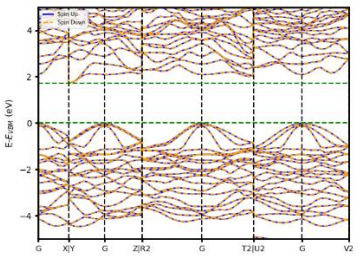

$NaCaGaP_2$

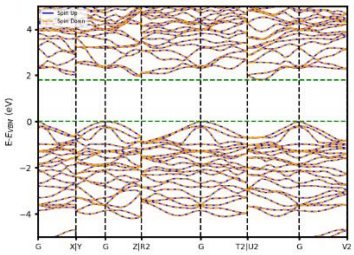

$NaCaInN_2$

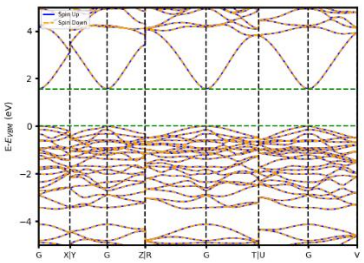

$LiCaInN_2$

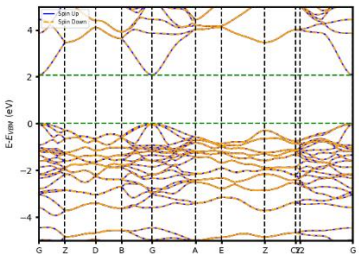

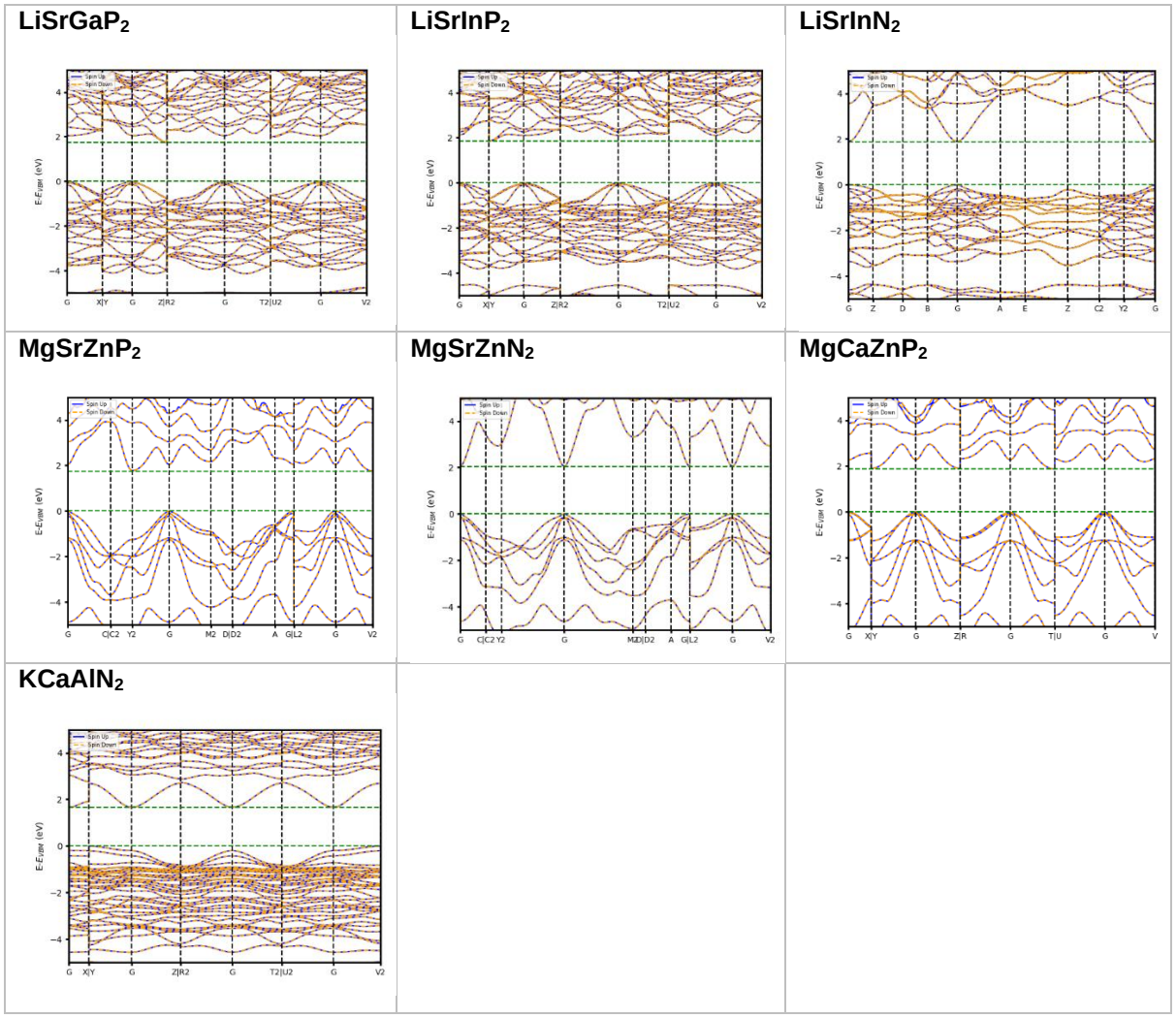

Figure 5: Band structure plots with each cell showing the compound considered and the energy eigenvalues (with respect to energy of VBM, E_{VBM}) along the path of high symmetry k-points of the Brillouin zone (in X-axis). The Gamma point is labelled as G in the X-axis. Vertical dotted lines show breaks in the k-path and horizontal lines show E_{VBM} and E_{CBM}. Dashed yellow lines show spin-down energies and blue lines show spin-up energies.

Like what is observed with DOS, the BB'B"X_2 show fewer bands per unit energy, making their band structure plots look less dense. Na_4ZnN_2 is predicted to be metallic, showing a band crossing the E_{VBM} and E_{CBM}. In this case, the horizontal green lines shown seem spurious as this compound has no band gap.

In order to observe the underprediction of the band gaps by SCAN compared to HSE06, we plot them as shown in Figure 6.

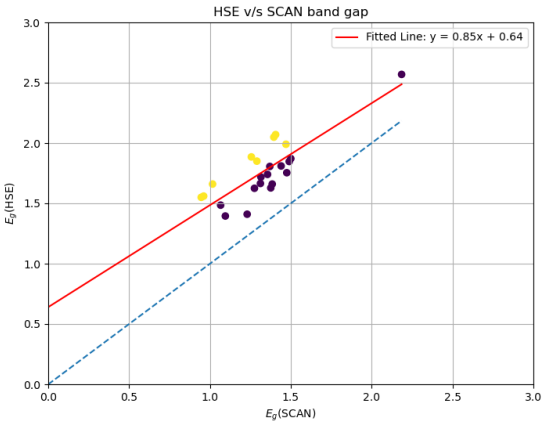

Figure 6: The HSE-calculated band-gap (Y-axis) versus the SCAN-calculated band-gap (X-axis) for the compounds whose band structures are calculated. The dotted line shows the y=x line, and the red line shows the line fit for the points. The yellow points indicate nitrides, and the purple points indicate phosphides.

From Figure 6, we infer that SCAN underpredicts band gaps (compared to HSE06) more for nitrides than phosphides. This could be due to the following hypothesis: due to the nitride ion having a concentrated negative charge and, therefore more localized electron density compared to a phosphide ion, nitrides show more self-interaction terms in the SCAN framework, leading to a lesser SCAN-predicted band gap compared to that with HSE06.

Table 13 shows the HSE06-calculated band gaps for the compounds and the band-gap type. The nearest direct band gap for the compounds with an indirect band-gap is shown.

Table 13: HSE06-calculated band gaps (E_g) for compounds with their composition class and type of band-gap. The rightmost column shows the nearest direct band-gap observed for indirect band-gap compounds. The compounds shaded in dark green have their direct band gaps in the range of 1.1 to 1.75 eV. The compounds shaded in light green have their nearest direct band gaps in the 1.1 to 1.75 eV range.

Class	Compound	HSE06 E_g (eV)	Type	Nearest direct E_g (eV)
$BB'B''X_2$	$MgSrZnN_2$	2.049	Direct	-
	$MgSrZnP_2$	1.754	Indirect	2.05
	$MgCaZnP_2$	1.871	Indirect	2.238
A_4BX_2	Na_4MgP_2	**1.41**	Direct	
	Li_4SrP_2	1.66	Indirect	2.5
	K_4ZnP_2	1.665	Indirect	**1.73**
	Na_4ZnN_2	-	Metallic	-
	Li_4ZnP_2	1.395	Indirect	2.3
	Na_4ZnP_2	1.628	Indirect	**1.657**

	Li_4ZnN_2	1.99	Indirect	2.96
	Li_4SrN_2	1.85	Indirect	2.09
$ABCX_2$	$NaCaInN_2$	**1.56**	Direct	-
	$LiCaInP_2$	1.81	Indirect	2.153
	$NaSrInN_2$	**1.55**	Direct	-
	$KCaAlN_2$	1.66	Indirect	1.833
	$LiZnInP_2$	1.485	Indirect	1.774
	$LiCaGaP_2$	1.718	Indirect	2.03
	$NaCaGaP_2$	1.806	Indirect	2.281
	$LiCaInN_2$	2.07	Direct	-
	$LiSrGaP_2$	1.74	Indirect	2.019
	$LiSrInP_2$	1.847	Indirect	2.14
	$LiSrInN_2$	1.885	Direct	-

As seen in Table 13, $NaCaInN_2$, $NaSrInN_2$ and Na_4MgP_2 show direct band gaps in the preferred range of 1.1 eV to 1.75 eV, with the direct band gap observed at their Gamma points. K_4ZnP_2 shows its VBM at Z (0, 0, 0.5) and CBM at Gamma (0, 0, 0). Na_4ZnP_2 shows its VBM at Y (0, 0.5, 0) and CBM at Gamma (0, 0, 0). However, both show direct band gaps at their Gamma points, which lie in the range of 1.1 eV to 1.73 eV. Therefore, we consider only these five compounds (of which three show direct band-gap) for calculating the effective mass of carriers and intrinsic defect formation energies.

In order to test the numerical procedure used to calculate the effective masses of electrons and holes, we test the code with the well-studied compound gallium arsenide (GaAs) [66], as shown in Table 14. For the hole effective mass, the valence band (the heavy band, showing less curvature) and the band below it (the light band, with higher curvature) intersect the valence band at VBM.

Table 14: Effective masses of hole (subscript h) and electron (subscript e) in units of mass of electron at rest for GaAs

	m_h^{eff} (light band)	m_h^{eff} (heavy band)	m_e^{eff}
Studies in [66]	-0.085	-0.45	0.067
Our calculation	-0.052	-0.43	0.056

As seen in Table 14, the errors in the effective mass occur only in the second decimal place, which is why we use the same code to calculate the effective mass of the carriers for the five considered compounds, as shown in Table 15.

Table 15: Effective masses of hole (subscript h) and electron (subscript e) in units of mass of electron at rest for the five compounds considered

Compound	m_h^{eff}	m_e^{eff}
Na_4MgP_2	-0.0245	0.1788
K_4ZnP_2	-39.3160	0.2767
Na_4ZnP_2	0.4559	0.2138
$NaCaInN_2$	-0.2585	0.1813
$NaSrInN_2$	-0.8934	0.1693

We see that the direct band-gap compounds $NaCaInN_2$ and $NaSrInN_2$ have lesser magnitudes of the electron effective mass, which can be verified by their conduction band showing more curvature at CBM, compared to the valence band at VBM. This means their free electrons are more mobile than their free holes at the band edges. Na_4MgP_2 shows the opposite trend of the electron effective mass is higher than that of the hole, signifying a lower mobility of free electrons than free holes. At the Gamma point, where the nearest direct band-gap lies for Na_4ZnP_2, it shows a positive effective mass of the hole, implying an upward-curved valence band at the point, which is verified from its band structure. This could reduce the hole mobility significantly, but the compound could be doped to make it n-type or used in a heterojunction, such that electrons cause the major current to have a significant photovoltaic performance. The close-to-flat valence band of K_4ZnP_2 gives it a nearest-direct band-gap value similar to its indirect band-gap value. However, the flatness of the valence band manifests as a significantly large magnitude of hole effective mass at the Gamma point, where its nearest direct band-gap lies.

3.5 Point defect formation energies

We calculate the intrinsic point defect formation energies for Na_4MgP_2 (in 2x2x1 supercell), Na_4ZnP_2 (in 2x2x1 supercell), K_4ZnP_2 (in 2x2x1 supercell), $NaCaInN_2$ (in 2x2x2 supercell) and $NaSrInN_2$ (in 2x2x2 supercell), and the results are shown in Table 16. The table shows only the defective configuration that shows the least energy for each defect type.

Table 16: The Defect formation energies of the five compounds. The column is the compound, with the second row showing the type of defect. Z-Y refers to the Z-Y antisite pair (Z_Y+Y_Z), and Vac_Y refers to a vacancy in Y site (X_Y), with the number of symmetrically unique combinations considered for defect type given in parenthesis

(no parenthesis means a single configuration considered). E_f is the defect formation energy with minimum (min) and maximum (max) values according to the chemical potential for the atom removed to create a vacancy. Antisite defects have a single value of E_f (“). Green shading represents values greater than 1 eV, yellow shading represents values very close to 1 eV, and red shading represents values less than 1 eV.

Compound	Defect	Supercell	E_f (min) (eV)	E_f (max) (eV)
$NaCaInN_2$	Ca-In		1.7053	"
	Ca-Na		0.7477	"
	In-Na		1.2546	"
	Vac_Na		1.0595	1.1151
	Vac_Ca		2.5592	2.5870
	Vac_In		3.9738	4.0016
	Vac_N (2)	2x2x2	0.6858	0.7229
$NaSrInN_2$	Na-Sr		0.9267	"
	Sr-In		2.5257	"
	In-Na		0.8758	"
	Vac_Na		1.1959	1.1969
	Vac_Sr		2.8634	3.0269
	Vac_In		3.5775	3.5785
	Vac_N (2)	2x2x2	0.5181	0.5997
Na_4MgP_2	Na-Mg (4)		-0.7998	"
	Vac_Na (4)		0.1888	0.6196
	Vac_Mg		0.1212	0.9837
	Vac_P (2)	2x2x1	-0.1302	1.1624
K_4ZnP_2	K-Zn (4)		2.4716	"
	Vac_K (2)		1.6392	2.0430
	Vac_P (3)		0.7612	1.8733
	Vac_Zn (2)	2x2x1	0.9587	2.0370
Na_4ZnP_2	Na-Zn (2)		1.5780	"
	Vac_Na (2)		1.2874	1.6682
	Vac_P		0.6384	1.6571
	Vac_Zn	2x2x1	2.1125	2.7504

In the table, the red-shaded defects are easier to form ($E_f < 1$ eV) and must hence be avoided. Since Na_4MgP_2 tends to form all the defects (with few being thermodynamically stable), we exclude its candidature as a prospective beyond-Si photovoltaic material. This tendency to form defects easily could be attributed to its metastability, as it is not a thermodynamically stable state. The formation of defects

could be a part of the underlying mechanism for its phase transformation to its thermodynamically stable state. Despite the other compounds showing a few defects that can form easily, the condition (chemical potential environment) in which the compound is synthesized could be altered so that defects do not readily form. For example, K_4ZnP_2 could be synthesized in a P-rich environment so that E_f(Vac_P) is maximized (using Le-Chatelier's principle of chemical equilibrium) and above 1 eV. Therefore, we conclude that $NaCaInN_2$, $NaSrInN_2$, K_4ZnP_2 and Na_4ZnP_2 are mostly resistant to form intrinsic defects.

3.6 Conclusion and Remarks

In this thesis, we computationally evaluate the pnictide compounds of $ABCX_2$, A_4BX_2 and BB'B"X_2 classes by initializing their structures, finding their stable polymorph, validating the thermodynamic stability of the more stable polymorph, analyze their electronic properties and confirm their resistance to form point defects in order to propose them as being prospective candidates for beyond-Si photovoltaics. We filter the compound space based on criteria applied to the properties at each stage of screening (thermodynamic stability, DOS, band structure and defect formation energy) and hereby conclude that **$NaCaInN_2$** ($P2_1/c$ space group), **$NaSrInN_2$** ($P2_1/c$ space group), **K_4ZnP_2** (R-3mH space group) and **Na_4ZnP_2** (R-3mH space group) can be prospective pnictide candidates for beyond-Si photovoltaics.

We point out that the chemical space of pnictides is restricted here without considering compositions with Group-XIV elements, many of which also satisfy the safety and abundance condition imposed when choosing the elements in the thesis. We initialized only two possible structures for each composition based on the experimentally observed structures of a few candidates and calculated all the other properties for these structures. However, this does not rule out the possibility of structures of other space groups for these compositions. Although hybrid functionals predict band gaps better than conventional functionals, they also underpredict band gaps. The band structure also changes when the compounds are doped or synthesized in other dimensions (for example, as nanosheets). We consider only intrinsic point defects of two types (single vacancy and cation antisite-pairs) in the study. Hence, this study

does not guarantee the complete resistance of the four candidate compounds towards forming defects, as we have not studied extrinsic, interstitial, and line defects.

Despite the caveats listed above, this study serves as a systematic filter to analyze the abilities of compositions in a new and relatively unexplored chemical space to be considered for further property-specific computation, experimental synthesis and device-level optimization. The dynamic (temperature-dependant) stability analysis using phonon modes, air (oxygen)-stability and moisture-stability of the compounds could be tested in further studies, along with the development of synthetic methodologies to form crystals of the four prospective compounds. After they are synthesized and characterized, dopants could be introduced to form homojunctions or heterojunctions to create scalable photovoltaic devices. We hope this thesis will be useful for further studies on the compounds analyzed and can be used to derive a workflow for similar research conducted in the future.

References

[1] National Geographic. (n.d.). Global warming effects. https://www.nationalgeographic.com/environment/article/global-warming-effects

[2] Britannica. (n.d.). Solar energy. https://www.britannica.com/science/solar-energy

[3] PV Education. (n.d.). Solar energy. https://www.pveducation.org/pvcdrom/introduction/solar-energy

[4] Shockley, W., and Queisser, H. (2018). Detailed balance limit of efficiency of p–n junction solar cells. *Renewable Energy* **2**, 35–54.

[5] Andreani, L.C., Bozzola, A., Kowalczewski, P., Liscidini, M., and Redorici, L. (2019). Silicon solar cells: toward the efficiency limits. *Advances in Physics: X* **4**, 1548305.

[6] Gautam, S.G., Canepa, P., Bo, S.-H., Ceder, G., and Wolverton, C. (2018). Novel solar cell materials: insights from first-principles. *The Journal of Physical Chemistry C* **122**, 27107–27126.

[7] Kumar, J., and Gautam, S.G. (2023). Study of pnictides for photovoltaic applications. *Physical Chemistry Chemical Physics* **25**, 9626–9635.

[8] Pizzini, S. (2010). Towards solar grade silicon: Challenges and benefits for low-cost photovoltaics. *Solar Energy Materials and Solar Cells* **94**, 1528–1533.

[9] Pizzini, S., and Calligarich, C. (1984). On the effect of impurities on the photovoltaic behavior of solar-grade silicon. *Journal of The Electrochemical Society* **131**, 2128.

[10] Gribov, B.G., and Zinov'Ev, K.V. (2003). Preparation of high-purity silicon for solar cells. *Inorganic Materials* **39**, 653–662.

[11] Ming, L.Y., Los, A., and Xiong, G. (2023). Thin film absorbers for tandem solar cells: an industrial perspective. *Journal of Physics: Energy* **5**, 042002.

[12] Berman, S., Gautam, S.G., and Carter, E.A. (2019). Role of Na and Ca as isovalent dopants in Cu_2ZnSnS_4 solar cells. *ACS Sustainable Chemistry & Engineering* **7**, 5792–5800.

[13] Zhu, J., and Pan, Y. (2024). Tunability of the electronic structure of GaN third-generation semiconductor for enhanced band gap: the influence of B concentration. *Materials Science and Engineering: B* **308**, 117554.

[14] Ščajev, P., Kauk-Kuusik, M., Grossberg, M., and Krustok, J. (2024). As-doped polycrystalline CdSeTe: localized defects, carrier mobility and lifetimes, and impact on high-efficiency solar cells. *Advanced Energy Materials* **2024**, 2403902.

[15] Green, M.A., Ho-Baillie, A., and Snaith, H.J. (2015). Optical properties of photovoltaic organic–inorganic lead halide perovskites. *The Journal of Physical Chemistry Letters* **6**, 4774–4785.

[16] Queisser, H.J., and Haller, E.E. (1998). Defects in semiconductors: some fatal, some vital. *Science* **281**, 945–950.

[17] Mahmood, A., and Wang, J.-L. (2021). Machine learning for high-performance organic solar cells: current scenario and future prospects. *Energy & Environmental Science* **14**, 90–105.

[18] Kusuma, F.J., Ikram, M., Othman, N.H., Yahya, M., and Salleh, N. (2025). Multi-properties prediction of perovskite materials using machine learning and meta-heuristic feature selection. *Solar Energy* **286**, 113189.

[19] Behera, G., Ganguly, S., Ahuja, R., and Jena, N.K. (2024). Ternary alkali-metal copper chalcogenides ACuX (A = Na, K; X = S, Se, Te): Promising candidates for harvesting solar energy. *Physical Review Applied* **22**, 024042.

[20] Casalegno, M., Bernardi, A., and Raos, G. (2013). Numerical simulation of photocurrent generation in bilayer organic solar cells: comparison of master equation and kinetic Monte Carlo approaches. *The Journal of Chemical Physics* **139**, 024002.

[21] Tully, A.B. (2023). From growth to TR-ARPES of C_{60}: a prototypical OPV system. PhD Dissertation, *University of British Columbia*.

[22] DiLeo, R.A., Zheng, Y., Xu, T., and Loo, Y.-L. (2007). Determination of nanomaterial energy levels for organic photovoltaics by cyclic voltammetry. *MRS Online Proceedings Library (OPL)* **1031**, 1031-H09.

[23] Wang, X., Lee, C., Hsu, W.C., and Yu, P.K. (2013). Design of GaAs solar cells operating close to the Shockley–Queisser limit. *IEEE Journal of Photovoltaics* **3**, 737–744.

[24] Todorov, T., Gunawan, O., Gokmen, T., Mitzi, D.B., and Guha, S. (2011). Progress towards marketable earth-abundant chalcogenide solar cells. *Thin Solid Films* **519**, 7378–7381.

[25] Zhou, Y., and Zhao, Y. (2019). Chemical stability and instability of inorganic halide perovskites. *Energy & Environmental Science* **12**, 1495–1511.

[26] Hossain, M.A., Rahman, K.S., Akhtar, M.S., and Karim, M.R. (2018). Electrochemical deposition of bulk MoS_2 thin films for photovoltaic applications. *Solar Energy Materials and Solar Cells* **186**, 165–174.

[27] Gautam, S.G., Canepa, P., Bo, S.-H., Ceder, G., and Wolverton, C. (2018). Novel solar cell materials: insights from first-principles. *The Journal of Physical Chemistry C* **122**, 27107–27126.

[28] Guo, D., Li, X., Wang, Y., Zhang, S., and Zhu, Y. (2017). Nanosheet-based printable perovskite solar cells. *Solar Energy Materials and Solar Cells* **159**, 518–525.

[29] Khazaei, M., Arai, M., Sasaki, T., Chung, C.-Y., and Sakka, Y. (2019). Recent advances in MXenes: from fundamentals to applications. *Current Opinion in Solid State and Materials Science* **23**, 164–178.

[30] Veerathangam, K., Pandian, M.S., and Ramasamy, P. (2018). Size-dependent photovoltaic performance of cadmium sulfide (CdS) quantum dots for solar cell applications. *Journal of Alloys and Compounds* **735**, 202–208.

[31] Fujiwara, H., Adachi, S., Kohara, N., and Harima, H. (2018). Organic-inorganic hybrid perovskite solar cells. *Spectroscopic Ellipsometry for Photovoltaics: Volume 1: Fundamental Principles and Solar Cell Characterization*, 463–507.

[32] Aumaitre, C., and Morin, J.-F. (2019). Polycyclic aromatic hydrocarbons as potential building blocks for organic solar cells. *The Chemical Record* **19**, 1142–1154.

[33] Kumagai, Y., Oba, F., Tanaka, I., and Murayama, M. (2023). Alkali mono-pnictides: a new class of photovoltaic materials by element mutation. *PRX Energy* **2**, 043002.

[34] Yao, Y., König, D., and Green, M. (2013). Investigation of boron antimonide as hot carrier absorber material. *Solar Energy Materials and Solar Cells* **111**, 123–126.

[35] Gruenbaum, P.E., Dinh, V.T., and Sundaram, V.S. (1994). Gallium antimonide infrared solar cells with improved efficiency and manufacturability. *Solar Energy Materials and Solar Cells* **32**, 61–69.

[36] Cakiroglu, D., Kaya, S., Yildirim, N., and Turan, R. (2019). Indium antimonide photovoltaic cells for near-field thermophotovoltaics. *Solar Energy Materials and Solar Cells* **203**, 110190.

[37] Zakutayev, A. (2016). Design of nitride semiconductors for solar energy conversion. *Journal of Materials Chemistry A* **4**, 6742–6754.

[38] Azzi, S., Toumi, L., Boukhechem, M.S., and Benramdane, N. (2023). Investigation of optoelectronic properties of half-Heusler KZnN and KZnP compounds. *Revista Mexicana de Física* **69**, 060501-1.

[39] Musembi, R., and Mbilo, M. (2022). *Ab initio* study of structural, electronic, elastic, mechanical, and optical properties of K_4XP_2 (X = Zn, Cd) compounds for optoelectronic applications. *Materialia* **26**, 101587.

[40] Kohn, W., and Sham, L.J. (1965). Self-consistent equations including exchange and correlation effects. *Physical Review* **140**, A1133.

[41] Kresse, G., and Furthmüller, J. (1996). Efficiency of *ab initio* total energy calculations for metals and semiconductors using a plane-wave basis set. *Computational Materials Science* **6**, 15–50.

[42] Hohenberg, P., and Kohn, W. (1964). Inhomogeneous electron gas. *Physical Review* **136**, B864.

[43] Sun, J., Ruzsinszky, A., and Perdew, J.P. (2015). Strongly constrained and appropriately normed semilocal density functional. *Physical Review Letters* **115**, 036402.

[44] Wexler, R.B., Gautam, S.G., and Carter, E.A. (2020). Exchange-correlation functional challenges in modeling quaternary chalcogenides. *Physical Review B* **102**, 054101.

[45] *The VASP Manual*. Available at: https://www.vasp.at/wiki/index.php/The_VASP_Manual.

[46] Blöchl, P.E. (1994). Projector augmented-wave method. *Physical Review B* **50**, 17953.

[47] Bergerhoff, G., Hundt, R., Sievers, R., and Brown, I.D. (1983). The inorganic crystal structure database. *Journal of Chemical Information and Computer Sciences* **23**, 66–69.

[48] Jain, A., Ong, S.P., Hautier, G., Chen, W., Richards, W.D., Dacek, S., Cholia, S., Gunter, D., Skinner, D., Ceder, G., and Persson, K.A. (2013). Commentary: The Materials Project: A materials genome approach to accelerating materials innovation. *APL Materials* **1**, 011002.

[49] Kirklin, S., Saal, J.E., Meredig, B., Thompson, A., Doak, J.W., Aykol, M., Rühl, S., and Wolverton, C. (2015). The Open Quantum Materials Database (OQMD): Assessing the accuracy of DFT formation energies. *npj Computational Materials* **1**, 15010.

[50] Draxl, C., and Scheffler, M. (2019). The NOMAD laboratory: From data sharing to artificial intelligence. *Journal of Physics: Materials* **2**, 036001.

[51] Bartel, C.J. (2022). Review of computational approaches to predict the thermodynamic stability of inorganic solids. *Journal of Materials Science* **57**, 10475–10498.

[52] Ong, S.P., Richards, W.D., Jain, A., Hautier, G., Kocher, M., Cholia, S., Gunter, D., Chevrier, V.L., Persson, K.A., and Ceder, G. (2013). Python Materials Genomics (pymatgen): A robust, open-source Python library for materials analysis. *Computational Materials Science* **68**, 314–319.

[53] Sun, W., Dacek, S.T., Ong, S.P., Hautier, G., Jain, A., Richards, W.D., Gamst, A.C., Persson, K.A., and Ceder, G. (2016). The thermodynamic scale of inorganic crystalline metastability. *Science Advances* **2**, e1600225.

[54] Lee, J. G. (2016). *Computational materials science: an introduction*. CRC press.

[55] Blöchl, P.E., Jepsen, O., and Andersen, O.K. (1994). Improved tetrahedron method for Brillouin-zone integrations. *Physical Review B* **49**, 16223.

[56] Slater, J.C. (1951). A simplification of the Hartree-Fock method. *Physical Review* **81**, 385.

[57] Krukau, A. V., Vydrov, O. A., Izmaylov, A. F., & Scuseria, G. E. (2006). Influence of the exchange screening parameter on the performance of screened hybrid functionals. *The Journal of chemical physics*, *125*(22).

[58] Wang, V., Xu, N., Liu, J.-C., Tang, G., and Geng, W.-T. (2021). VASPKIT: A user-friendly interface facilitating high-throughput computing and analysis using VASP code. *Computer Physics Communications* **267**, 108033.

[59] Wang, V., Guo, M., Liu, J.-C., and Geng, W.-T. (2022). High-throughput computational screening of two-dimensional semiconductors. *The Journal of Physical Chemistry Letters* **13**, 11581–11594.

[60] Barrett, P., Hunter, J., Miller, J.T., Hsu, J.-C., and Greenfield, P. (2005). *Matplotlib—A Portable Python Plotting Package*. *Astronomical Data Analysis Software and Systems XIV*, **347**.

[61] Memming, R. (2015). *Semiconductor electrochemistry*. John Wiley & Sons.

[62] Virtanen, P., Gommers, R., Oliphant, T.E., Haberland, M., Reddy, T., Cournapeau, D., Burovski, E., Peterson, P., Weckesser, W., Bright, J., and van der Walt, S.J. (2020). SciPy 1.0: Fundamental algorithms for scientific computing in Python. *Nature Methods* **17**, 261–272.

[63] Freysoldt, C., Grabowski, B., Hickel, T., Neugebauer, J., Kresse, G., Janotti, A., and Van de Walle, C.G. (2014). First-principles calculations for point defects in solids. *Reviews of Modern Physics* **86**, 253–305.

[64] Johnson, E. (1996). The calculation of electrostatic potentials for periodic charge distributions. *The Journal of Chemical Physics* **105**, 5529–5531.

[65] Hinuma, Y., Pizzi, G., Kumagai, Y., Oba, F., and Tanaka, I. (2017). Band structure diagram paths based on crystallography. *Computational Materials Science* **128**, 140–184.

[66] Kim, Y.-S., Kang, Y., and Walsh, A. (2010). Towards efficient band structure and effective mass calculations for III-V direct band-gap semiconductors. *Physical Review B—Condensed Matter and Materials Physics* **82**, 205212.